7-10-2024

Large Length Scale Droplet Capillary Phenomena: Generation, Jump, and Capture

Karl Jeffrey Theodore Cardin
Portland State University

Large Length Scale Droplet Capillary Phenomena:

Generation, Jump, and Capture

by

Karl Jeffrey Theodore Cardin

A dissertation submitted in partial fulfillment of the
requirements for the degree of

Doctor of Philosophy
in
Mechanical Engineering

Dissertation Committee:
Raúl Bayoán Cal, Chair
Christophe Josserand
Jay Nadeau
Howard A. Stone
Derek Tretheway

Portland State University
2024

Abstract

Understanding the life cycle of droplets, from generation to capture, for example, is critical to understanding environments from the air-sea interface to the indoor environment of the International Space Station. Investigations have been performed in this work to provide insight into three droplet phenomena, each ubiquitous in both terrestrial and microgravity settings, through a lens of capillary flow. Each investigation attempts to disentangle the effects of gravity from the effects of surface tension. A drop tower test campaign is performed for each of the three investigations. Models are developed and simulations are performed to rationalize the observations. Each investigation is outlined below.

The first investigation considers a droplet impacting a fiber array. Droplets interacting with fiber arrays is common in nature, textiles, microelectromechanical devices, and fog harvesting. The phenomena of droplet impact on an equidistant array of fibers is experimentally studied. Drop tower tests are performed to characterize the droplet dynamics in the absence of the effects of gravity which could deform fibers and bias equilibrium configurations. Results show that contact line dissipation is largely responsible for arresting the droplet. Additionally, the penetration length is affected by fiber flexibility. A model is developed predicting the droplet penetration dynamics which shows good agreement with experiments.

The second investigation considers the jump of a droplet from a particle bed. Drop Tower experiments have been performed investigating droplet jump from a particle bed across a wide range of fluid viscosities. The presence of a particle layer

is shown to affect contact line dissipation of the jumping droplet. Additionally, the study has identified the impact of the Ohnesorge number (Oh) on droplet morphology. The investigation has yielded results that not only validate a modified version of the spring-mass-damper model proposed by Jha et al.[1] but also extend its applicability to previously unexplored initial conditions. In particular, the model predicts droplet jump time and velocity. Moreover, the presence of particle layers has been found to effectively eliminate contact line dissipation without introducing substantial additional forms of dissipation. Experiments have been conducted at the Dryden Drop Tower facility at Portland State University.

Lastly, the collapse of an air jet blown cavity and subsequent generation of a jet and jet droplets is investigated both experimentally and numerically. It is shown that surface tension forces alone are sufficient to generate a liquid jet from the cavity collapse. The dependence of the properties of the resulting liquid jet and jet droplets on the initial cavity geometry are discussed. Axisymmetric simulations of the Navier-Stokes equations for a simplified geometry are performed to look more closely at the evolution of the cavity geometry.

Acknowledgements

Financial support for this work has been provided in part by a NASA Space Technology Research Fellowship (NSTRF) under grant 80NSSC19K1191.

I thank Mark Weislogel for supervising the work for the first two years. I am grateful to Raúl Bayoán Cal for supervising the second half of the PhD and giving me the opportunity to present this work at multiple occasions. Thanks to Christophe Josserand for many fruitful discussions and for hosting me at LadHyX in the summer of 2022. I thank the members of the labs at Portland State University as well as NASA Glenn who supported me in many ways, academic or otherwise. I also thank the other members of my supervisory committee Jay Nadeau, Howard A. Stone, and Derek Tretheway for agreeing to evaluate this dissertation.

This work would not exist without the unfailing support of my family. I have immense gratitude for the foundation you have provided.

Table of Contents

List of Tables

List of Figures

Chapter 1

Introduction

In our daily lives capillary phenomena are primarily observed at millimetric scales. Regardless of this limitation, capillary phenomena are ubiquitous from water droplets on a rain jacket to water striders walking on a pond. Surface tension forces sculpt the world as we know it. However, even on millimetric scales, surface tension forces are in constant competition with gravitational forces. In this chapter a range of such phenomena will be introduced and the relevant dimensionless groups will be highlighted followed by a discussion of microgravity experimentation.

Consider the impact of rain on a pine tree, Fig. 1.1. A droplet on a pine needle migrates to the bottom side of the needle due to the droplets weight. If the needle and droplet were much smaller, or the gravity they experience less, the droplet might adopt an axisymmetric shape. One can also consider the impact process which deposited the droplet on the needle and consider what role gravity played and how the droplet dynamics would be different in the absence of gravity. How would droplets be distributed on the tree foliage if gravitational settling did not dominate the problem?

The size of rain droplets suspended from pine needles depends on the relative

Figure 1.1: Photograph showing the distribution of water droplets on a pine tree following a period of rain. Terrestrial gravity, g_0, vector is included for reference.

role of gravitational forces to surface tension forces which may be characterized by the Bond number

$$Bo \equiv \frac{\Delta\rho g l^2}{\gamma}, \tag{1.1}$$

where $\Delta\rho$ is the difference in density between the two fluids, g is the gravitational acceleration, l is the characteristic length, and γ is the surface tension. $Bo \ll 1$ is required for surface tension to play a dominant role compared to gravity.

Setting the Bond number to unity one can extract the capillary length

$$l_c \equiv \sqrt{\frac{\gamma}{\Delta\rho g}}. \tag{1.2}$$

The terrestrial capillary length for water is 2.5 mm. For terrestrial systems with a characteristic length of approximately l_c, both gravity and surface tension forces

must be considered. For terrestrial systems with a characteristic length $\gg l_c$, surface tensions effects will be negligible.

Similarly, one could consider a droplet impacting a granular bed, Fig. 1.2(a). In a terrestrial environment, surface tension plays a subdominant role. To increase understanding of such processes, it is natural to ask what role exactly surface tension is playing. One way to characterize the ratio of droplet inertia to surface tension is through the Weber number

$$We \equiv \frac{\rho R v^2}{\gamma}.$$

Another phenomena where gravity often plays a dominant role is the collapse of an air cavity in water. Such cavities can, for example, be generated by impacting a free surface with a solid body as shown in Fig. 1.2(b) [3]. The collapse dynamics in this study were shown to be largely a function of the Froude number

$$Fr \equiv \frac{v}{\sqrt{gl}}$$

which compares inertial and gravitational forces.

When gravity plays a subdominant role, in environments such as the International Space Station, for example, our intuition, built from a lifetime of experience of terrestrial gravity, often fails. With the increased use of video cameras on the International Space Station, examples of such counterintuitive phenomena are readily available to view online. Figure 1.3 shows three frames from a video of astronaut Scott Kelly placing an effervescent tablet in a sphere of water. A few things to note:

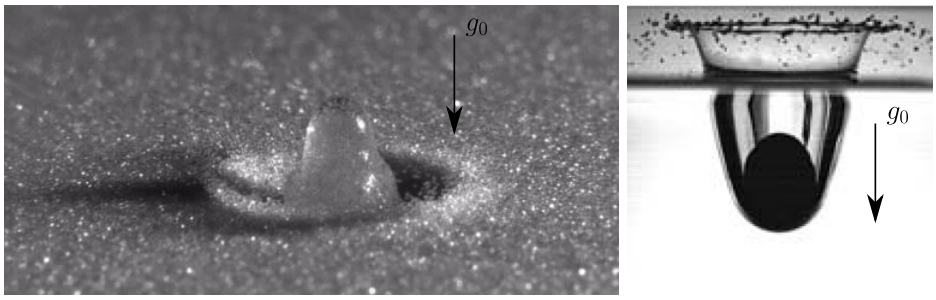

(a) (b)

Figure 1.2: (a) Photograph showing Impact of a water drop on a granular surface [2]. (b) A solid sphere impacting a liquid bath and creating a cavity in its wake. Terrestrial gravity, g_0, vector is included for reference in each image. [3].

the bubble are not driven any particular direction due to buoyancy, the bubble are quite stable because there is minimal film drainage [9], in the middle frame a huge liquid jet has emerged from a bursting bubble, and on the right frame a jet droplet is observed.

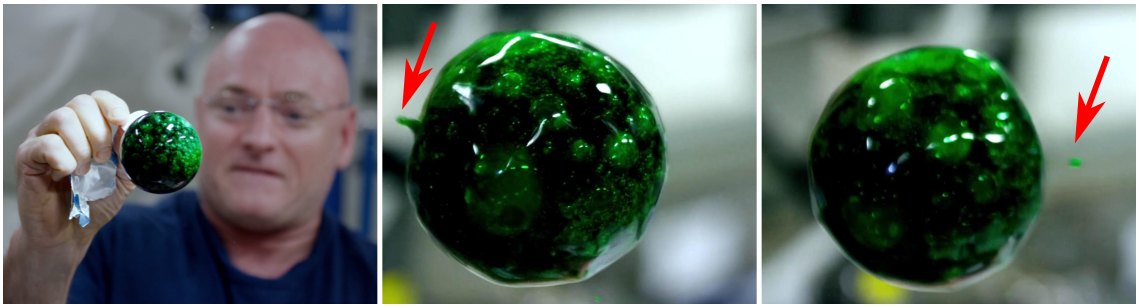

Figure 1.3: Frames from video of astronaut Scott Kelly adding an effervescent antacid tablet into a ball of dyed water on the International Space Station.

When considering a free surface flows such as the bubbles bursting in Fig. 1.3, often the Laplace number is considered. The Laplace number is the Reynolds number

based on the capillary wave speed γ/μ:

$$La = \frac{\gamma \rho l}{\mu^2} \tag{1.3}$$

The Laplace number defines regimes for processes such as atomization and jet breakup. The same dimensionless group is often refereed to as the Suratman number Su. There is an additional related dimensionless group the Ohnesorge number $Oh = 1/\sqrt{La}$.

One might assume that understanding the fluid mechanics of terrestrial systems below the capillary scale lacks applications. However, many industries rely on surface tension driven dynamics. For example, the microfluidics industry has exploited capillary flows extensively. This industry is in a rapid growth phase. This growth is highlighted in Baban et al. [10]:

> *The global microfluidics market is projected to be worth 58.8 billion USD, growing at a compound annual growth rate (CAGR) of 23.2% with the biochip (lab-on-a-chip and microarrays) market projected to register a CAGR of 13.9% during the period of 2022–2027.*

Internal flows in such devices are almost always laminar as characterized by the Reynolds number

$$Re = \frac{\rho v l}{\mu}, \tag{1.4}$$

where μ is the dynamic viscosity and v is a characteristic velocity.

Just a few examples among myriad problems where surface tensions plays a significant role have been highlighted. Advances are continually being made in un-

derstanding how these often overwhelmed surface tension forces shape the world. Capillary fluidics is a rich area of research which spans the spectrum from fundamental to applied science. To answer such a question, disentangling the forces due to gravity and surface tension, requires unique efforts.

Microgavity environments are incredibly useful for studying capillary flows. In discussion of these environment, and in this document, the colloquial terms "microgravity," "low-gravity," and "weightless" are often used although these terms are generally inaccurate. Although "weightlessness" is how an astronaut might describe the environment of the International Space Station, gravity at 300 km above the Earth's surface is only slightly less than at sea level ($9.37\,\mathrm{m\,s^{-2}}$ compared to $9.81\,\mathrm{m\,s^{-2}}$ at sea level). The fact that the space station is in free fall, rather than a reduction in gravity, is what makes the environment "weightless". Most methods of microgravity experimentation rely on a frame of reference which is in free fall.

In an attempt to study large length scale capillary fluidics, given the form of l_c, one might try to increase γ or decrease $\Delta\rho$. However, water has the highest surface tension $0.072\,\mathrm{N\,m^{-1}}$ of common working fluids only exceeded by mercury $0.438\,\mathrm{N\,m^{-1}}$. Modifying $\Delta\rho$ was the approach taken by Plateau [11]. However, such a method is limited my difficulties in precisely matching fluid densities to achieve micro-gravity levels, as well the limitations of choices in immiscible fluids.

In an environment where $g = 10^{-4}g_0$, for example, the capillary length for water becomes $\mathcal{O}(1\,\mathrm{m})$. As a result, tasks such as predicting the location of a liquid propellant in a tank with $l \sim 1\,\mathrm{m}$ (dynamically and in equilibrium), such as is often found on spacecraft, requires an intimate understanding of capillary fluidics. The desire to

control fluids in orbiting vehicles (propellants, life support systems, etc.) supported the development and refinement of systems which allow for microgravity experimentation. A summary of the primary methods for microgravity experimentation are provided below.

A sounding rocket launch can provide 6-13 minutes of microgravity time. Sounding rocket payloads usually fly between two and three years after experiment approval [12]. Although exact numbers are difficult to find, each launch easily exceeds one million dollars. During the flight there is limited interaction with the experiments. One benefit of sounding rocket flights is much less stringent safety requirements than experiments on the International Space Station.

Spacecraft in low earth orbit also provide a microgravity environment. The International Space Station provides access to long duration, minutes to years, microgravity. Experiments can be controlled via telemetry by researchers on Earth or be manually operated by astronauts on board the International Space Station. These experiment often have high costs and long lead times. Additionally, meeting the rigorous experiment safety standards provide a significant hurdle.

Airplanes can fly in a series of parabolic ascents and descents which provide $\sim$22 s of low gravity for each cycle. Such flight trajectories are difficult to achieve and require two skilled pilots and a mechanic: first pilot vertical load factor at zero, the second pilot maintains the roll angle at zero, and a mechanic controls the longitudinal load factor [13]. A sequence of these cycles can be performed to provide $\sim$10 minute of low-gravity time per scientific flight. On hyperbolic flights the operators can interact directly with the experiment. Additionally, experiments

with human subject are possible. Operating a low-gravity flight is expensive with a single research flight will cost at least $55,000 [14].

Drop tower experimentation offers a low coast option for micogravity research. The main disadvantage of drop towers is the limited microgravity time that they provide. Two of the premiere drop tower facilities in the world are at NASA Glenn and Zarm which provide 5.18 s and 4.74 (9.3 s in catapult mode) of microgravity time, respectively [15, 16]. Each of these towers evacuate the air from the facility before performing the drop tower test so that the drop package does no experience air resistance. The drop tower used in this work will be discussed in Chapter 2.

Working at length scales greater than the terrestrial capillary length scale provides a multitude of experimental benefits. These benefits span imaging, experiment manufacturing, and unique initial conditions.

The larger capillary lengths available in drop tower experiments enable easier visualization than terrestrial experiments. Complex imaging set ups with extension tubes and macro lenses are less often required. Additionally, the time scales associated with such conditions are also greater allowing for slower video frame acquisition frequencies.

Performing experiments at scales below terrestrial capillary length scales often required special manufacturing techniques. For example, lab-on-chip prototypes are often made from polydimethylsiloxane by cold casting. This transparent polymer is cast from a two-part mixture at low temperatures over a mould. poly(methyl methacrylate) (PMMA) is another material often used in microfluidic devices. PMMA is often manufactured for such devices using micromachining, laser

ablation, or microinjection molding. In contrast, for drop tower experiments, off the shelf components, traditional manufacturing methods, 3d-printing, laser cutting, water jet, etc can all be easily employed.

Another trait which separates drop towers from other methods of simulating microgravity in the apparent step reductions in gravity. While other method may provide longer microgravity duration, the experiment is exposed to many different accelerations through the transportation process. The apparent step reduction in gravity at the beginning of a drop tower test, Fig. 2.1 point 1, allows for unique experiments. For example, this step reduction is gravity has been used to provide fascinating results in the case of droplet jump where a droplet deposited on a superhydrophobic substrate leaves the substrates as the fluid surface reorients in response to the step reduction in gravity [7]. A detailed overview of the drop tower used in this work, the Dryden drop tower at Portland State University, is provided in Chapter 2.

With this foundation laid, the motivation of the three investigations presented herein can be established. Each investigation takes advantage of the unique low gravity environment of the drop tower to investigate a droplet phenomena. Broadly the studies are concerned with the topics of droplet capture, droplet interaction, and droplet generation. These topics are highly applicable to environment control on spacecraft where sedimentation cannot be relied on to remove large droplets from the air. Aerosol samplers deployed on the International Space Station have shown the presences of a wide variety of environmental contaminants [17]. At the same time, each project is quite fundamental and the insight can shed light on terrestrial

systems as well. In chapter 2 background on the methods used in these investigations is provided. Chapter 3, 4, and 5 present studies on droplet capture in a fiber array, droplet jump from a particle bed, and cavity collpase, respectively. The document concludes by presenting future work in chapter 6.

Chapter 2

Methods

2.1 Dryden Drop Tower

The Dryden Drop Tower (DDT) is a safe, low-cost, high-rate facility located in the atrium of an engineering building on the Portland State University campus. An image of the tower is provided in Figure 2.3. The drop tower can be operated by a single person so the experiment operator has full control of the experiment right up to the release of the drop package.

A graph of the typical acceleration of an experiment rig in shown in Fig. 2.1. During a drop test, the rig and drag shield are released simultaneously, Fig. 2.1 point 1, and do not make contact throughout the microgravity period of the drop tower test; because the rig is enclosed in the drag shield, the rig is largely protected from aerodynamic drag during free fall. The free fall period where $g < 2 \times 10^{-4} g_0$ lasts 2.1 s, Fig. 2.1 region 2.

Because the drag shield is slowed by aerodynamic drag, the initial 0.2 m gap between the bottom of the experiment rig and the floor of the drag shield reduces until the experiment rig makes contact with the drag shield some time before the

drag shield enters the magnetic braking system, Fig. 2.1 point 3. At the end of each drop tower test, slender ferrous fins on each side of the drop capsule enter a magnetic field which decelerates the capsule at a max $> 14g_0$, Fig. 2.1 point 4. After being decelerated the drag shield gently settles past the magnets and lands on foam pads Fig. 2.1 points 5 and 6.

Once the drag shield is resting on the foam pads at the bottom of the tower, the retrieval process can begin. An automated retrieval system attached to a winch is lowered down the drop tower shaft. Once the retrieval system reaches the drag shield, a latching mechanism attaches to the drag shield, the winch rotation is reversed, and the drag shield is pulled to the top of the drop tower. As the drag shield reaches the top of the tower the winch slows and then stops. At this point, the operator can secure the drag shield in a safety stand and begin preparing the next drop. This retrieval process takes just couple minutes.

The ease of use and accessibility of the Dryden Drop Tower makes it unique. Drop tower tests can be performed by a single operator. Because the drop tower uses a drag shield, rather than other methods of negating the effects of air resistance such as vacuum, the turn around time between drop tests is minimized. This combined with the automated retrieval system described above means that drop tower test can be performed approximately every five minutes. Indeed, over one hundred test have been performed in a single day.

Despite many unique benefits, the experimental environment of a drop tower provides many unique challenges. One of the primary challenges is the size and mass constraints of the experimental platform. The experimental campaigns conducted

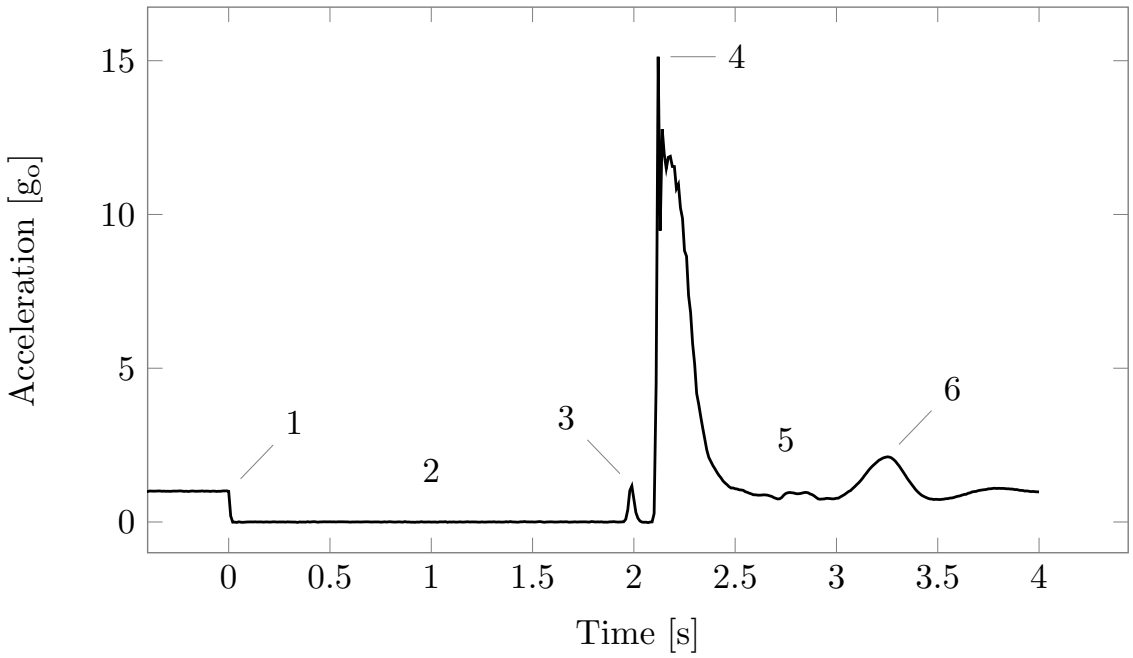

Figure 2.1: Sequence of drop tower acceleration events during a drop tower test: (1) drag shield and experiment rig release, (2) 2.1s low-g period, (3) experiment rig makes contact with the floor of drag shield, (4) drag shield enters permanent magnet field and is decelerated at $\sim 14g_0$, (5) drag shield achieves terminal velocity in magnets $\sim 1g_0$, and (6) drag shield lands on foam padding $\sim 2g_0$. Plot from Wollman [4].

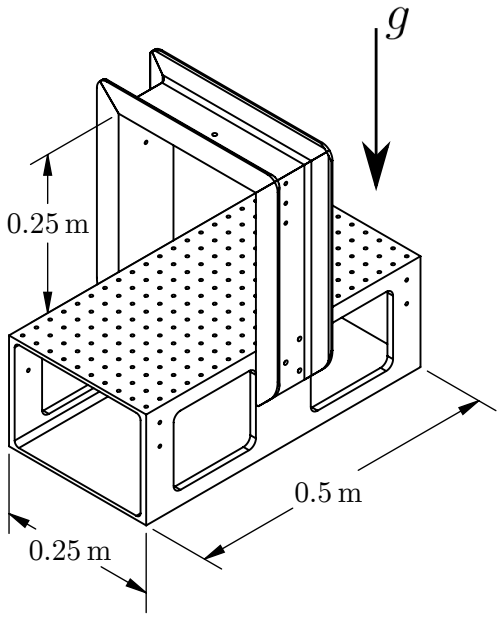

Figure 2.2: Drawing of the experiment rig used for the investigations in this research.

for the work in this document were performed using a multi purpose experiment rig as shown in Fig. 2.2. The top platform in a *breadboard* with 1/4"-20 holes on a 2.54 cm grid. The experiment is largely constrained to the 0.25×0.25×0.5 m volume above the threaded platform. All electric components (solenoids, backlight, cameras, etc.) must be battery powered. The batteries are placed on the bottom platform of the experiment rig. To ensure the rig doesn't rotate during the drop tower test, it must be precisely leveled in the plane perpendicular to the gravity vector g. The total weight of the experiment rig must remain below 400 N. Since the cameras are also mounted to the threaded substrate, the maximum working distance of the lens is approximately ∼0.5 m.

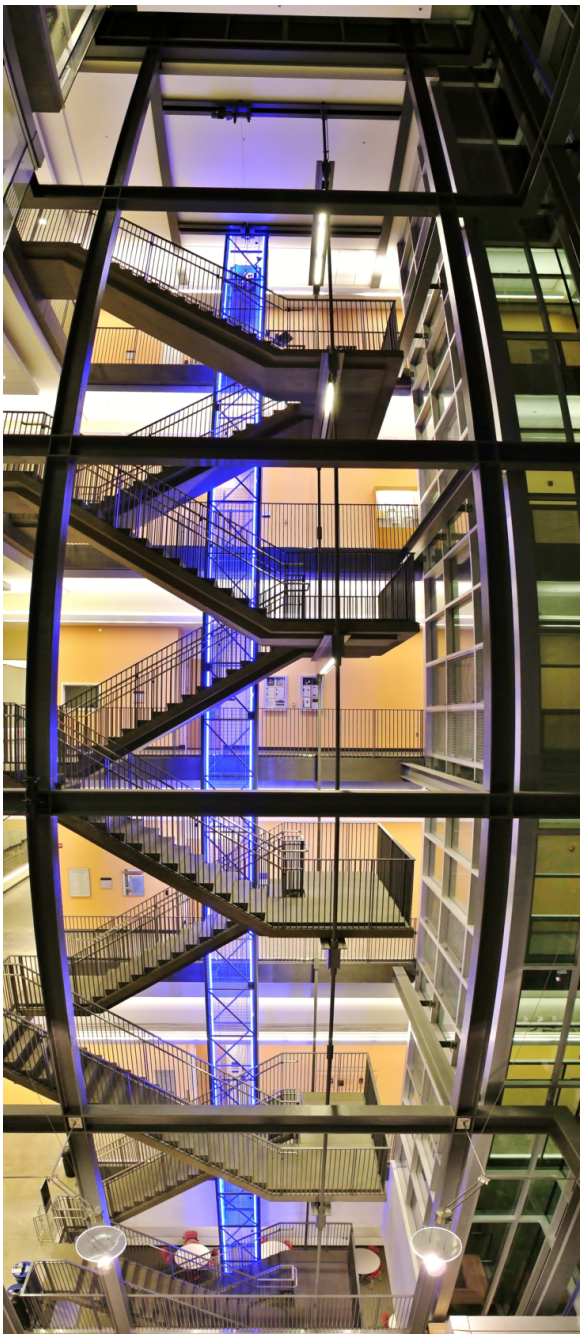

Figure 2.3: Photo of the five story Dryden Drop Tower at Portland State University. Photo from Wollman and Weislogel [5].

2.2 Superhydrophobic substrate

The droplet impact study required the development of a new method to accurately impact a target with a droplet. The droplet jump mechanism [7] was employed to achieve this. However, the super-hydrophobic substrates used in previous studies were not able to accurately located the droplet before each drop tower test to ensure impact with the intended target.

In Attari et al. [7] surface roughness was generated by either laser etching acrylic sheets using a 60W CO2 Universal Laser Systems VLS4.60 or by 3D printing the substrate with a 30 μm resolution 3D Systems Projet 3500. Once the substrates were manufactured, they were coated with a low surface energy coating Dome Magic purchased from King Controls. Droplet jump for volumes 0.04–400 ml was investigated. A maximum jump velocity of 0.12 m/s which was achieved for a 2 ml droplet on a laser etched substrate. Later, surfaces were manufactured by adhering sandpaper to a rigid base substrate and coating the sandpaper with a low surface energy coating. These sandpaper based substrates were used to investigate the rebound of a water jet from a superhydrophobic substrate [6], Fig. 2.4, and viscous droplet jump Juboori [8].

Each of these methods provided a unique downside. The localized heating from the laser etching process tended to warp the acrylic substrate. 3D printing required out of house manufacturing and long lead times. The sandpaper was limited to flat substrates. Accurately positioning a droplet on a such a superhydrophobic surface on the free hanging test rig was prohibitively difficult. For these reasons a new

Figure 2.4: Image from a drop tower test showing a 6 mm diameter jet impacting and rebounding from a sandpaper based super hydrophobic substrate [6].

method of creating superhydrophobic substrate was pursued.

The base substrate for the superhydrophobic substrates used herein is a double concave lens with 50cm focal length. The lens is coated with Glaco Mirror Coat Zero purchased from Soft99 Co. Three coats of the glaco are applied to the lens. The lens is dried at 150°C for half an hour between each coat. The water contact angle on this substrate is $\theta = 160°$.

Fig. 2.5 shows images from a drop tower test for a 2ml water droplet jumping from a superhydrophobic concave lens. The droplet jump velocity is 0.12 m/s. The jump velocity agrees with the maximum jump velocity attained in the investigation of Attari et al. [7] for a 2 ml droplet. This method of creating a slightly concave superhydrophobic surface has now been used in multiple studies which require accurate control of the droplet impact position in a drop tower test.

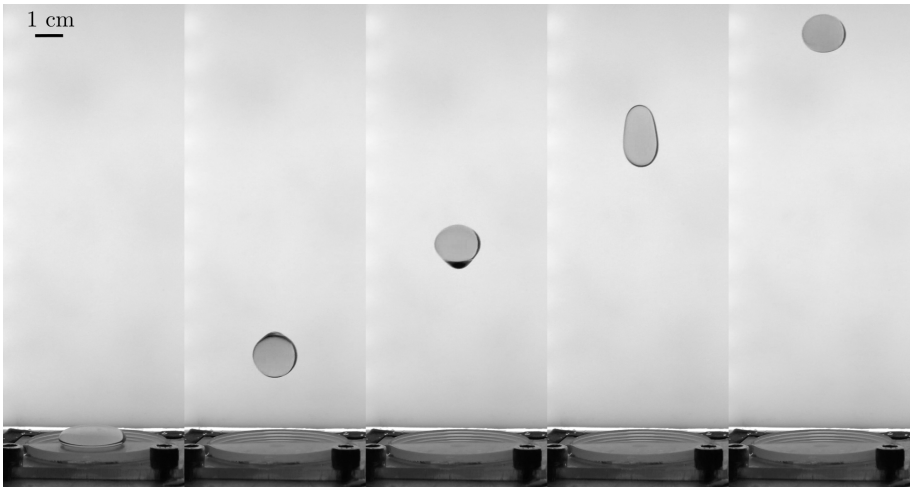

Figure 2.5: Images from a drop tower test showing a 2 ml water droplet jumping from a concave superhydrophobic substrate.

2.3 Numerical method

The Basilisk computational fluid dynamics code is used in this work to investigate two-phase flow with surface tension. Basilisk uses the finite volume method to solve the Navier-Stokes equations directly. The numerical scheme is described in detail in Popinet [18] and Popinet [19]. The Basilisk code has been used previously for a variety of problems including bubble bursting at a free surface [20–22].

The dynamics of the two fluids are governed by the unsteady incompressible, variable density, Navier-Stokes equations which can be written:

$$\partial_t \mathbf{u} + \nabla \cdot (\mathbf{u} \otimes \mathbf{u}) = \frac{1}{\rho} \left[-\nabla p + \nabla \cdot (2\mu \mathbf{D}) + \mathbf{F}_\gamma \right] \tag{2.1}$$

$$\partial_t \rho + \nabla \cdot (\rho \mathbf{u}) = 0 \tag{2.2}$$

$$\nabla \cdot \mathbf{u} = 0 \tag{2.3}$$

Where $\mathbf{u}$ is the velocity, p is the pressure, ρ the fluid density, μ the fluid viscosity, $\mathbf{F}_\gamma$ the surface tension force, $\mathbf{D} = [\nabla \mathbf{u} + (\nabla \mathbf{u})^T]/2$ is the rate of deformation tensor. The surface tension force is $\mathbf{F}_\gamma = \gamma k \delta_s \mathbf{n}$ where δ_s is a surface Dirac δ-function that is nonzero only on the interface, γ is the surface tension, k is the curvature, and $\mathbf{n}$ is the normal to the interface Popinet [19].

A variable c is introduced to differentiate the liquid phase from the gas phase. c describes the volume fraction of the liquid phase in each cell. c=0 if the cell contains

only gas, c=1 if the cell contains only liquid and $1 < c < 0$ if the cell contains the interface. The value of c is defined in each cell throughout the simulation. The density and viscosity can then be defined by:

$$\rho(c) = c\rho_{\text{liq}} + (1 - c)\rho_{\text{gas}} \tag{2.4}$$

$$\mu(c) = c\mu_{\text{liq}} + (1 - c)\mu_{\text{gas}} \tag{2.5}$$

For each cell containing an interface, the interface normal $\mathbf{m}$ is stored in addition to the volume fraction c. The position of the interface can be uniquely determined from the interface normal and volume fraction. For details on the piecewise-linear geometrical Volume Of Fluid (VOF) scheme used in basilisk, see Popinet [19].

Another defining feature of the basilisk software is adaptive mesh refinement. An example of the quadtree mesh structure is provided in Fig. 2.6. Specific refinement criteria can be defined by the user in the code. The adaptive mesh refinement allows simulations to be performed with significantly less computational resources than a uniform Cartesian mesh. An example of the evolution of a mesh throughout a simulation is presented in Fig. 2.7.

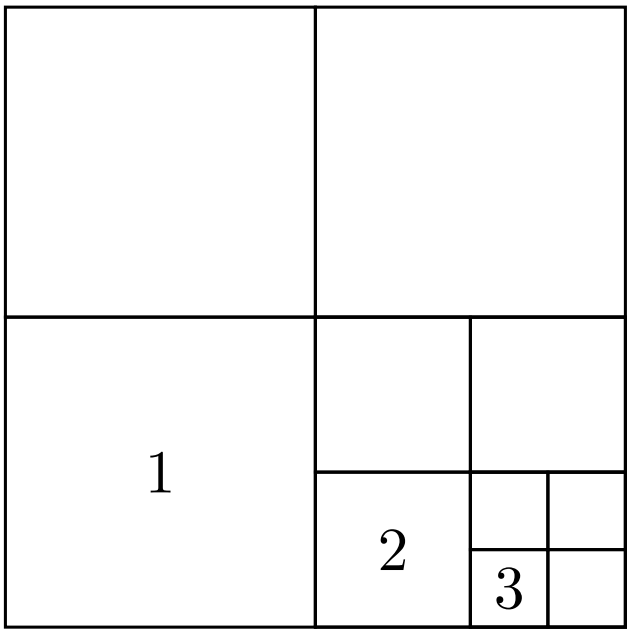

Figure 2.6: Depiction of quadtree mesh structure. A single cell has been divided to contain 3 different level of mesh. Neighbors of any cell at levels l must be level $l \pm 1$.

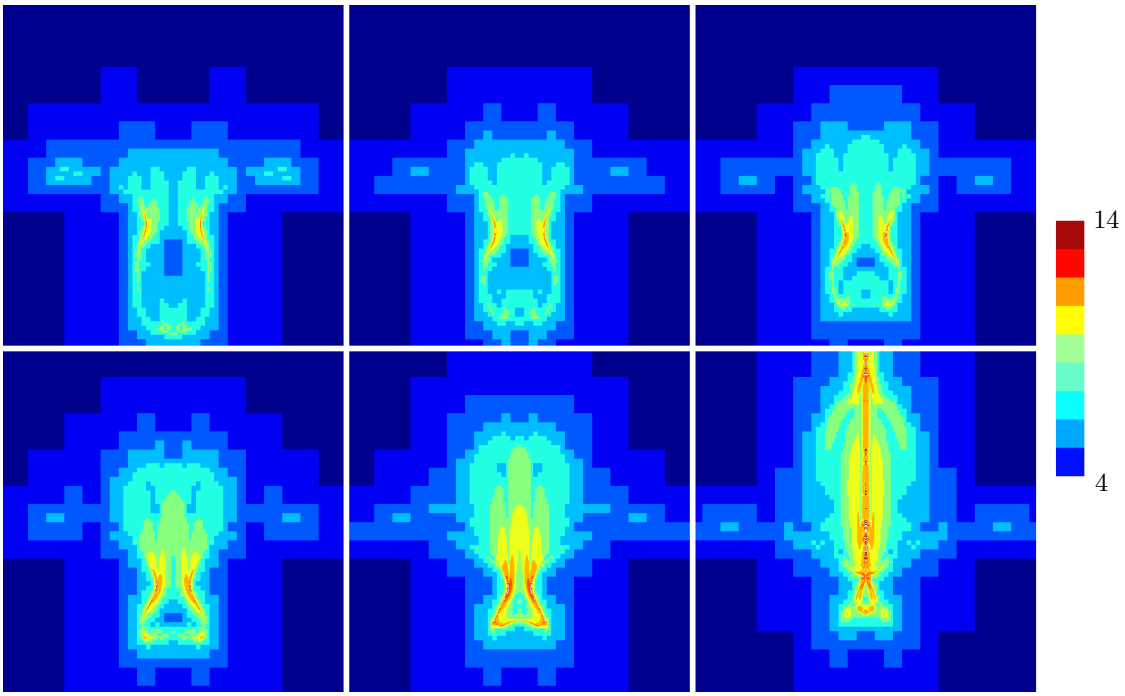

Figure 2.7: Evolution of resolution level for the cavity collapse simulations performed in the study presented in Chapter 5.

Chapter 3

Droplet Capture in a Fiber Array

3.1 Introduction

The interaction of droplets with slender structures is ubiquitous in both nature and technology. Nature has utilized fiber arrays for functions such as rejecting condensed water droplets from the legs of water striders using flexible setae to maintain flotation [23] and water collection by plants in arid environments [24–27]. Taking inspiration from nature, arrays of stretched fibers have been shown to effectively recover water from fog [28]. Understanding the interaction between capillary forces and the deformation of structures such as carbon nanotube carpets is important for the manufacturing of microelectromechanical devices [29]. The effects of structure, wettability, flexiblity, etc. on the ability of a fiber structure to capture

This chapter is based on the article:
Karl Cardin, Christophe Josserand, and Raúl Bayoán Cal. Droplet capture in a fiber array. *Physical Review Fluids*, 8(4):043601, 2023.

a droplet and the final equilibrium configuration of the droplet remain rich areas of research.

Drop impacts on horizontal fibers, where the droplet velocity is normal to the fiber axis, have recently received much attention while on-axis impacts have lagged behind. The critical velocity threshold between capture and fragmentation was quantified for inviscid droplets impacting a fixed fiber [30]. The critical velocity of capture increases for a droplet impacting an angled fiber [31]. Studies of Drop impact on horizontal flexible fibers demonstrate that droplet capture efficiency can be increased by modifying the fiber flexibility [32, 33]. Nasto et al. [34] used energy arguments to identify a variety of regimes for on-axis droplet impact on fiber arrays constructed from casting Polydimethylsiloxane.

Insight into the equilibrium configurations of liquid bodies in fiber arrays is valuable for its relevance to many applications such as fog harvesting and textile manufacturing. Investigations have examined the equilibrium configuration of liquid bridging multiple fibers [35–41]. Princen [38] predicted the cross-sectional shape of liquid columns between various equidistant arrays of cylinders, neglecting gravity, for a range of contact angles. Protiere et al. [40] investigated the transition between column and attached droplet configurations for perfectly wetting drops between two rigid cylinders finding dependence on the drop volume, cylinder radius, and cylinder spacing. Duprat et al. [41] showed that elasticity promoted droplet spreading between flexible fibers. The clustering of many fibers as they are withdrawn from a bath of wetting liquid has also been studied [42, 39].

Previous studies of droplets traveling on fibers have focused on the visco-capillary

systems. Such systems include droplets travelling along a conical fiber where the gradient is droplet curvature drives the motion while viscous dissipation resists the motion [43]. A similar case of a bubble traveling along a fiber submerged in a bath of liquid has also been investigated where the dynamics are dominated by buoyancy and viscous dissipation [44].

Here, a visco-inertial system of droplet penetration and capture in a fiber array is studied - a regime which is unique to mesoscale fibers [34]. Additionally, challenges of manufacturing and experimental imaging that an experiment with micro liter droplets would encounter are circumvented. By utilising the unique low gravity environment of a drop tower the fibers are free from gravity induced deformations. Such experiments inform technologies such as water recovery from aerosols in space which will be critical for long duration space travel. In addition to the relevance to low gravity technologies, such experiments will help to disentangle the different contributions to terrestrial droplet penetration dynamics. In particular, droplet dynamics and equilibrium configurations will not be affected by the droplet and fiber weights. This paper is outlined as follows: The drop tower experimental apparatus is discussed, then data from a large drop tower test campaign is presented, finally models are presented which predict the penetration length of a droplet into a fiber array.

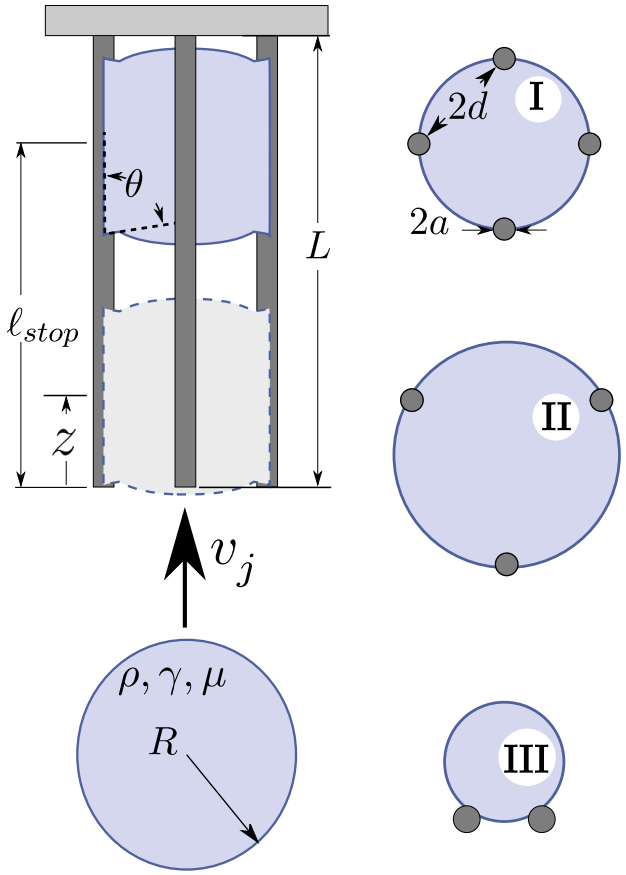

Figure 3.1: Diagram of a droplet impacting a fiber array with relevant parameter shown and illustrations of relevant fiber array patterns: square (I), triangular (II), line (III).

3.2 Methods

Figure 3.1 shows a diagram of the fiber impact experiment with relavent parameters indicated. Nylon monofilament fishing line or stainless steel rod of diameter $2a$, ranging from 0.1-0.8 mm, is used for the fibers. Nylon fibers are straightened by threading through glass capillaries with inner diameter $\sim 2a$ [45] and then placing

in an oven at 50-100 °C for a minimum of 5 minutes. Straightened fibers of length L are attached in patterns with edge-to-edge distance $2d$ to a fixture plate which allows them to be accurately positioned centered over the droplet at the beginning of the drop tower test. The static contact angle θ of the fibers is determined to be $\sim$60 deg from inspecting the contact line of droplet in equilibrium during drop tower tests.

The drop jump mechanism [7] is used to generate impacting droplets. A concave superhydrophobic substrate is create by coating a concave lens with Glaco Mirror Coat (Soft 99). The resulting substrate has a static contact angle of 165 deg. Before each drop tower test, a volume, $(4/3)\pi R^3$, of fluid with density ρ, surface tension γ and dynamic viscosity μ is deposited onto the superhydrophobic substrate using a syringe. Water with a small amount of dye added for visualization is used as the working fluid. The slight curvature of the superhydrophobic surface allows more accurate positioning of the droplet. At the beginning of the drop tower test, following the step reduction in gravity, the excess surface energy of the droplet is transferred into kinetic energy causing the droplet to travel away from the superhydrophobic substrate and towards the fiber array at the jump velocity v_j. During the drop tower test, the droplet impacts the fiber array, travels along the fibers, and either stops at a distance ℓ_{stop} or travels the full fiber length and impacts fixturing plate. Additional details regarding the droplet jump mechanism are provided in Attari et al. [7].

All experiments are imaged at 120 fps with 1920×1080 pixel resolution using consumer-grade Panasonic cameras model HC-WX970. A diffuse LED array is

Parameter	Symbol	Range
Density	ρ	$1.0\,\mathrm{g\,cm^{-3}}$
Surface tension	γ	$72\,\mathrm{mN\,m^{-1}}$
Viscosity	μ	$0.89\,\mathrm{mPa\,s}$
Drop radius	R	3.6-7.8 mm
Drop jump velocity	v_j	$8.6\text{-}15.6\,\mathrm{cm\,s^{-1}}$
Number of fibers	n_f	2-13
Fiber length	L	22-73 mm
Fiber radius	a	0.1-0.8 mm
Fiber spacing	d	0.6-3.4 mm
Contact angle	θ	60°

Table 3.1: The parameter regime explored in this experimental study of droplets impacting fiber arrays.

adopted to backlight the phenomena. Droplet velocities, droplet equilibrium positions, fibers deflections, etc. are extracted from video using image analysis software Fiji [46].

3.3 Model

Typical snapshots of the droplet impingement on the fibers (here, three fibers) are shown in Figure 3.2 for illustration. There, the droplet penetrates into the fibers array, where it decelerates until it stops at a given length. It is important to emphasize here that, in the absence of gravity, the different forces that can explain the arrest of the droplet are the viscous, the capillary and the elastic ones. However, since we observe almost no fiber deformation at equilibrium and that the capillary forces almost balance each other after the drop wets the fibers (there should be in fact a small difference between the advancing and receding contact angle, that we

can neglect here), in the model below only the viscous dissipation is considered.

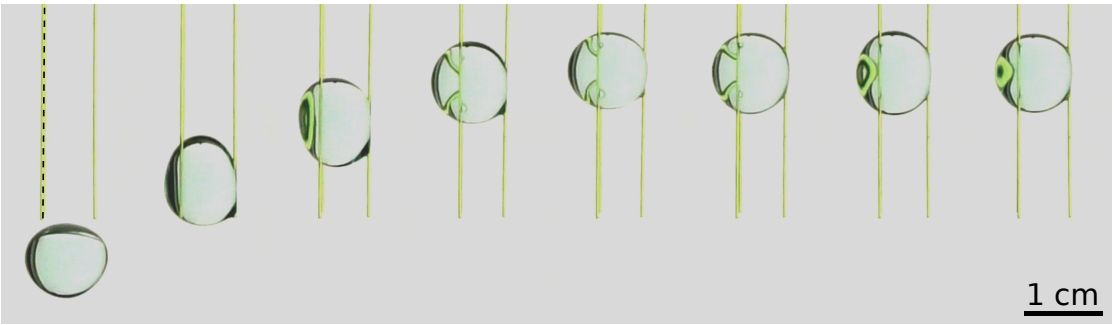

Figure 3.2: Montage from a drop tower test showing a 0.25ml droplet entering a three-fiber array. The location of the third, not clearly visible, fiber is depicted by the dashed line.

Then, assuming simple droplet and meniscus geometries, we can deduce a model where viscous dissipation is the main physical ingredient for the dynamics at first approximation. Viscous forces are proportional to the gradient of the velocity which are very high close to the contact line, so that one can usually consider that the viscous dissipation can be decomposed in two distinct contributions, one coming from the the velocity gradient in the bulk, the other from the motion of the contact lines along the fiber [47–49]. Therefore, to predict the penetration of the droplet into the fiber array, these two forms of viscous dissipation are considered, one which acts in the fluid bulk and the other along the droplet contact lines on the fibers. Near the moving contact line, the viscous force is given by [47]

$$\mathrm{F}_{cl} = \ell_{cl}\frac{3\mu\dot{z}}{\theta}\ln(\frac{\ell_M}{\ell_m}), \tag{3.1}$$

where z is the droplet center height (and thus $\dot{z}$ the vertical velocity of the drol-

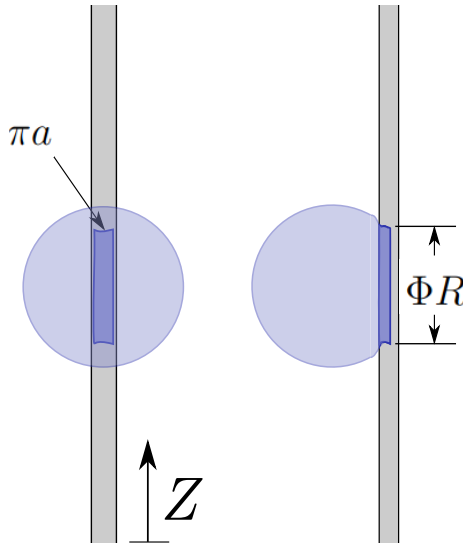

Figure 3.3: Diagram showing the simplified contact region of a droplet attached to a single fiber. Such a contact region is assumed for each fiber.

plet, see Figure 3.1), ℓ_M and ℓ_m are the macroscopic and microscopic cutoff sizes, respectively. We choose the characteristic distance between fibers for the macroscopic cutoff we take $\ell_M \sim 1$ mm and the molecular size for the microscopic cutoff $\ell_m \sim 1$ Å, therefore we take $\ln(\ell_M/\ell_m) \simeq 16$. Considering Figure 3.3, the contact length ℓ_{cl} can be written as,

$$\ell_{cl} = n_f 2(\pi a + \Phi R), \tag{3.2}$$

where Φ is a free parameter which accounts for the length of the contact line along the fiber. Additionally, we consider a bulk viscous force F_{bulk} resulting from the fluid between each set of nearest-neighbour fibers. The velocity gradient between two neighboring fibers is of the order $\dot{z}/d$, so dissipation is of the order $\mu\dot{z}/d$. We will consider this force to act over the contact area shown in Figure 3.3. The bulk

viscous force is therefore expressed as

$$\mathrm{F}_{bulk} = A_c \mu \frac{\dot{z}}{d}, \tag{3.3}$$

defining A_c considering Fig. 3.3 as

$$A_c = n_f(\pi a \Phi R), \tag{3.4}$$

where n_f is the number of fibers that the drop encounters.

The relative magnitude of the two dissipation terms is

$$\frac{F_{cl}}{F_{Bulk}} = \frac{\ell_{cl}}{A_c} \frac{3d}{\theta} \ln\left(\frac{\ell_M}{\ell_m}\right). \tag{3.5}$$

For the fiber arrays studied in this work the contact line dissipation dominates

$$\frac{F_{cl}}{F_{Bulk}} > 1 \tag{3.6}$$

For the fiber array geometries explored, $d/a > 1$, droplet wicking between fibers is expected to be minimal [38] and the droplets are expected to remain largely spherical, or in the 'drop' configuration [40].

For the forces considered, Newton's law of dynamics can be written:

$$\frac{d}{dt}\left(M\dot{z}\right) + F_{cl} + F_{bulk} = 0, \tag{3.7}$$

where M is the mass of the droplet. Substituting Eq. 3.1 and Eq. 3.3 into Eq. 3.7,

letting

$$\zeta = \frac{1}{M}\left(\ell_{cl}\frac{3\mu}{\theta}\ln(\frac{\ell_M}{\ell_m}) + A_c\frac{\mu}{d}\right), \tag{3.8}$$

and considering initial conditions $z(0) = 0$ and $v(0) = v_0$ yield the solution

$$z(t) = \frac{v_0}{\zeta}\left(1 - e^{-\zeta t}\right). \tag{3.9}$$

Since the liquid wets the fiber, the drop is somehow accelerated when entering the fiber array and a prediction of the initial velocity v_0 can be constructed using an energy argument. The droplet kinetic energy after entering the fiber array is thus

$$\varepsilon_{k,2} = \varepsilon_{k,1} + \varepsilon_\gamma, \tag{3.10}$$

where

$$\varepsilon_{k,1} = (1/2)Mv_j^2 \tag{3.11}$$

and ε_γ is the difference of the surface energy between the drop-fibers system before and after the penetration. In the view that this final kinetic energy corresponds to the initial velocity v_0 of the droplet to be considered in the model, it yields:

$$v_0 = \sqrt{v_j^2 - \frac{2}{M}\varepsilon_\gamma}. \tag{3.12}$$

Due to the droplet remaining largely spherical, the change in surface energy can be estimated simply by neglecting the variation of the droplet surface so that only the

wetted parts of the fibers $A_{S,G\to L}$ have to be considered leading to

$$\varepsilon_\gamma = A_{S,G\to L}\left(\gamma_{SG} - \gamma_{SL}\right) \tag{3.13}$$

where $A_{S,G\to L}$ is the fiber area that becomes covered by liquid, γ_{SL} is the solid/liquid surface tension, and γ_{SG} is the solid/gas surface free energy. The energy transformed to surface energy depends on the geometry of the fiber array. Using these assumptions and the Young equation,

$$\gamma_{SL} - \gamma_{SG} = -\gamma\cos\theta \tag{3.14}$$

where $\cos\theta \approx 1/2$ for the fibers used, the surface energy becomes

$$\varepsilon_\gamma = -n_f(\pi a\Phi R)\gamma\cos\theta. \tag{3.15}$$

Finally, Eq. 3.9 with Eq. 3.12 provides a complete prediction for the droplet trajectory with a single free parameter Φ.

3.4 Results

Initially we will discuss three-fiber arrays as they are the most basic array geometry that can capture a droplet in the inter-fiber volume. The fiber spacing is chosen such that confinement is small for 0.25 ml droplets, $d \sim R$. Even with nylon fibers, only small amplitude $A < R$ fiber oscillations occur after droplet impact for the

three-fiber arrays. Trajectories from Eq. 3.9, with unique optimum values of Φ, are plotted against measured z positions in Figure 3.4. Droplet z positions are tracked from when the centroid is at the free end of the fiber array until the end of the drop tower test. A typical progression of a droplet into a fiber array is presented in Figure 3.2. Droplet centroid locations are measured by fitting an ellipse to the droplet boundary. Predicted penetrations length agree well with experiments with an error between Eq. 3.9 at $t = 2.1$ s and the measured penetration length ℓ_{stop} of 8% on average. An average value $\Phi = 2.76$ is found for 0.25 ml droplets with a variance of 1.1. When using this average value of Φ the average error increases from 8% to 23%.

Letting $\Phi = 2.76$, the measured penetration length of all tests, with parameter ranges outlined in table 3.1, are compared to Eq. 3.9 at $t = 2.1$ in Fig. 3.5. The largest variation in behavior is for two-fiber arrays. This can be attributed to unpredictable behavior due the the lack of symmetry and confinement. The model tends to over predict the penetration for droplet with volume greater than 0.25 ml. This over-prediction is likely partially due to a larger contact line length caused by increased droplet confinement.

For two-fiber arrays, the droplet is not constrained to any inter-fiber volume. For these tests the droplet reaches an asymmetric equilibrium as a droplet attached to the side of both fibers, see Fig 3.6(a). The most flexible fibers arranged in arrays of two fibers are shown to respond to drop impacts with large amplitude $A \sim R$ multi-mode fiber oscillations which are much larger than those observed for stainless steel fibers in an array of the same geometry, Figure 3.6(b). For large amplitude

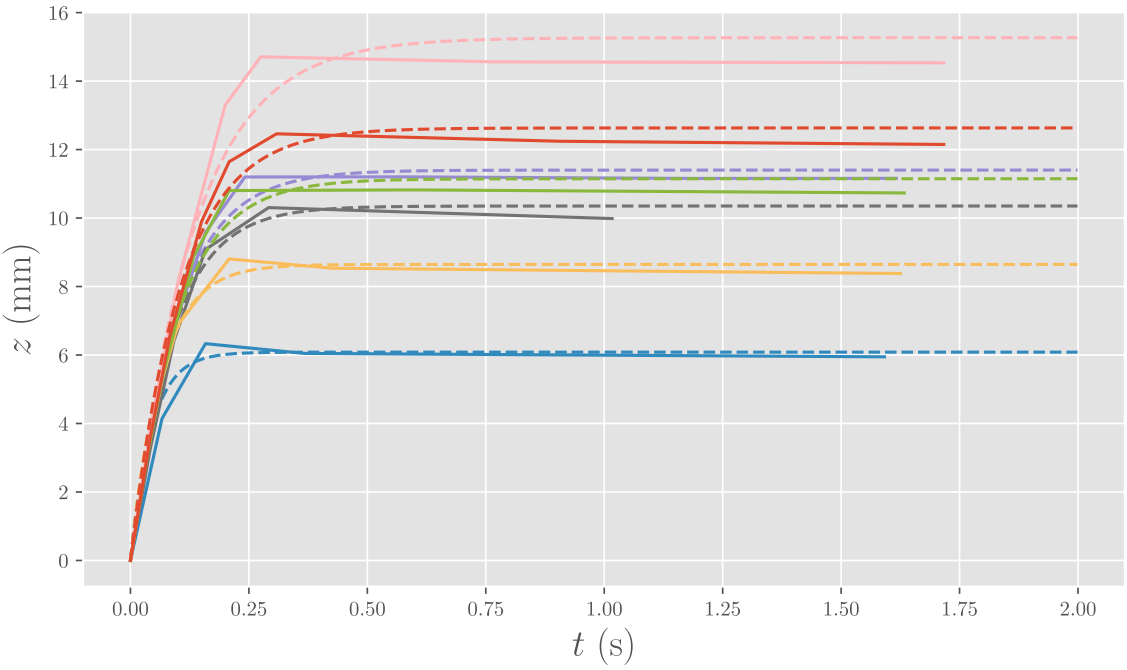

Figure 3.4: Experimental measurements (solid) compared to equation Eq. 3.9 (dashed) with optimum values of Φ for 0.25ml droplet and three-fiber configurations. $F_{cl}/F_{Bulk} \sim 300$ for these cases. Colors are to distinguish between individual drop tower tests.

oscillations, the contact length of the droplet grows and shrinks during each cycle. The contact line movement resulting from fiber oscillations was measured for various drops and found to be comparable to the penetration length. Therefore, the contact line dissipation associated with the fiber oscillations is expected to play a significant role in reducing the final penetration length for the more flexible fibers.

For the fiber arrays in the line configuration the fibers briefly pierce the droplet until the droplet migrated to one side of the fiber array. The force associated with the fiber piercing the droplet is assumed to be small for the limited number of small diameter fibers considered, and no significant deviation from the model is observed

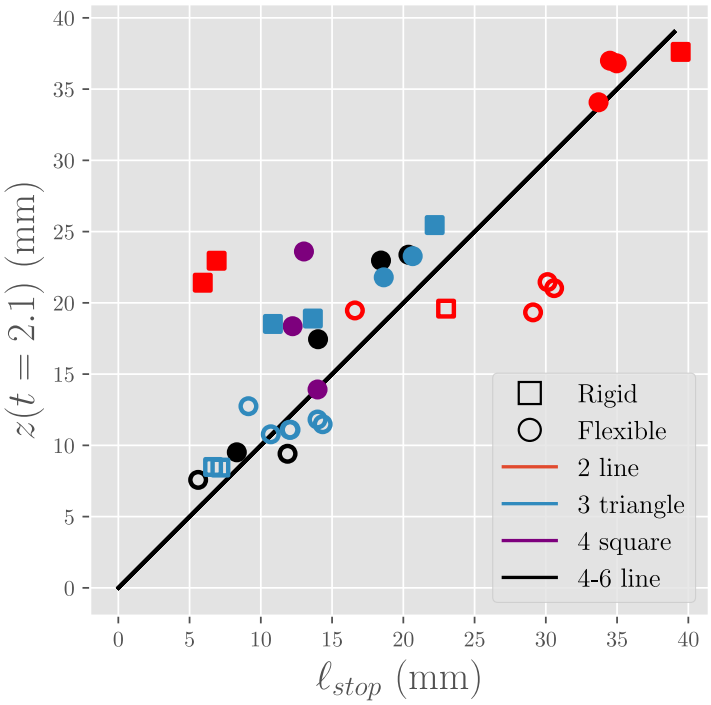

Figure 3.5: Comparison between predicted and measured penetration length for a wide variety of fiber arrays with $\Phi = 2.76$. Open symbols are for 0.25 ml drops and filled symbols are for drops with 0.25 ml $<$ volume $\leq$ 1.0 ml.

for these arrays. However, the model would have to be extended to capture the dynamics of penetration into fiber arrays which have many fibers which continually pierce the droplet. The case of a fiber piercing an interface has been considered in Neukirch et al. [50] and Raufaste et al. [51]. A test of such a configuration is shown in Fig. 3.6(c). Further study of arrays with piercing fibers is left to future investigations.

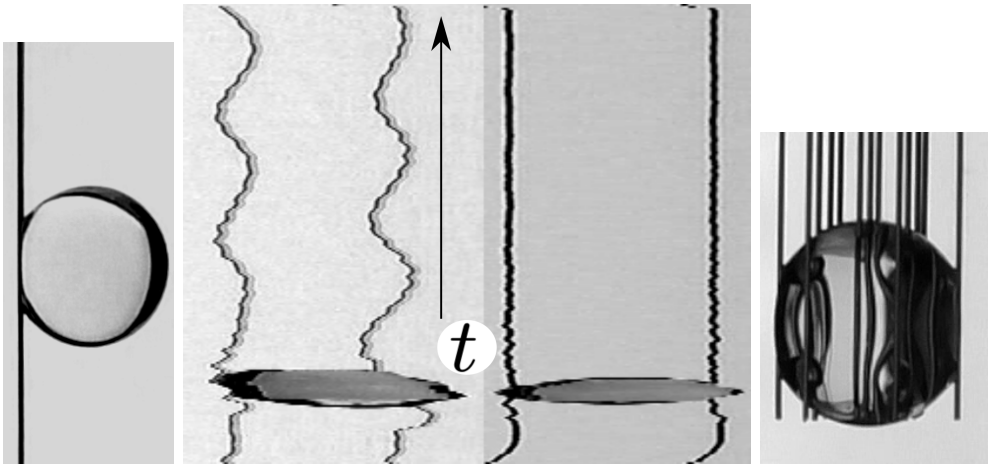

(a) (b) (c)

Figure 3.6: (a) Asymmetric equilibrium configuration of a 0.5 mL droplet on a two-fiber array. (b) Kymograph (spatiotemporal diagrams) sampling the free end of the fiber showing fiber response to 0.25 mL droplet for flexible (left) and rigid (right) two-fiber arrays (c) Droplet equilibrium position in a hexagonal fiber array with six fibers on the droplet periphery and seven fibers piercing the droplet.

3.5 Discussion

A model based on dynamics which are dominated by viscous dissipation has been presented which can predict the penetration length of a droplet into a fiber array. By comparison with impact experiments performed in a drop tower, the model is shown to be robust over a wide range of parameters. Such a simple model has the advantage to capture the main findings of our experiments, indicating that viscous dissipation at the contact lines in particular controls the drop motion in the fibers array. A more complex model should take into account capillary terms and fiber elasticity in particular, and the complex geometry of the drop as it penetrates the fibers. It might improve the quantitative comparisons with the experiments but at

the cost of higher complexity, so that it is postponed to further investigations.

How the penetration length of a droplet in a fiber array can be altered by modifying the fiber properties and fiber arrangement is also studied here. It is shown that fibers which exhibit large amplitude oscillations reduce the penetration length relative to rigid fiber arrays of the same geometry. Additionally, this work presents a novel perspective on the static equilibrium configurations of fluid bodies in fiber arrays in the absence of gravity. For line configurations of fibers, the transition from a symmetric impact to an asymmetric equilibrium configuration as an off-center attached body is observed, Fig. 3.6(a). The results of this work provide insight for applications such as fog harvesting, textile manufacturing, anti-spalsh substrates, and microelectromechanical devices.

Chapter 4

Droplet Jump From a Particle Bed

4.1 Introduction

Droplet-substrate interactions may seem like a mundane occurrence in our everyday lives: from raindrops hitting the ground to water splashing in a sink. However, the study of droplet impact holds immense importance and has far-reaching implications that are yet to be fully understood. The core of works in the topic focus on drop rebound; specifically, the most fundamental scenario of droplet impact on a flat, rigid substrate [1, 52, 53]. In recent years, the body of work has been extended to include compliant substrates [54]. Nevertheless, natural and industrial substrates are often covered with a granular substrate such as dust, sand, spores, etc. It is unclear how the presence of the latter might affect the droplet impact process.

This chapter is based on the article:
Karl Cardin, Facundo Cabrera-Booman, and Raúl Bayoán Cal. Droplet jump from a particle bed. *Soft Matter*, 20(13):2887–2891, 2024.

This is an exciting scientific endeavor as droplet interactions with dirty surfaces are central to understand processes including erosion [55], disease spread within crops [56], solar panel cleaning [57], among many others.

The impact of a droplet on a sufficiently hydrophobic substrate may be followed by the droplet rebounding from the substrate. Such a rebound can be considered in two stages. In the first stage, the droplet spreads, flattens, and reaches maximal radial extension. In the second stage, the flattened droplet retracts and rebounds from the substrate. Numerous studies have looked at water droplet rebound from superhydrophobic substrates [58, 48, 59]. Specially, Jha et al. [1] studied the rebound of viscous droplets from a super hydrophobic surface and developed a model for droplet rebound time and coefficient of restitution.

Droplet jump is physically similar in its phenomenology to the second stage of droplet rebound. The experimental procedure for droplet jump is as follows: a substrate which exhibits high liquid mobility for the test fluid is placed in the drop rig. A liquid volume is deposited on the substrate and allowed to settle to its equilibrium shape in the presence of gravity. The drop rig is released and the free fall starts, subjecting the liquid to an apparent step reduction in gravity. The liquid reorients towards its new equilibrium shape in the absence of gravity and jumps from the substrate.

Note that before the jump occurs, the droplet is in equilibrium with no internal flow which is in contrast to the case of drop rebound where a recirculating flow is may be present near the rim of the spreading droplet [60]. Attari et al. [7] studied water droplet jump from superhydrophobic substrates. Notably, they studied volumes in

the range $0.04 - 400$ ml, and showed that, by considering the change in droplet surface energy, the jump velocities could be reasonably predicted for volumes $0.5 \lesssim V_d \lesssim 2$ ml. More recently, Juboori [8] extended the data of Attari et al. [7] by considering the jump of viscous glycerol solutions. Droplet jump has been used as a mechanism to generate droplets for the study impact phenomena in drop towers [7, 61].

When particles are added to the substrate from which the droplet jumps, the problem becomes more complex albeit closer to reality. For instance, drop impact on granular substrates has received significant attention with particular interest in crater morphology [62–66, 2, 67]. Marston et al. [68] Investigated the initial dynamics of liquid drop impact onto particle beds and obeserved regimes of spreading, rebound, splashing and powder ejectas. Supakar et al. [69] focused on the spreading of water droplets onto particle beds and subsequent formation of liquid marbles (i.e. volumes of water completely encapsulated by particles) during impact onto hydrophobic powder surfaces. They identified a variety of resulting configurations including partial coverage, full encapsulation with spherical liquid marbles, and frozen deformed liquid marbles across a broad range of parameters.

Here, droplet jump from a particle bed is investigated. Drop Tower experiments are performed for two different particle sizes. The drop rebound model of Jha et al. [1] is extended to droplet jump from a particle bed and shown to be in agreement with experiments. The effects of the particle bed are discussed, including contact line dissipation during the retraction phase of droplet jump as well as particle size effects.

This investigation provides a unique platform to explore a large range of dimensionless parameters relevant to the problem via a Drop Tower. The presented experiment provides an ideal scenario to study fundamental drop jump behavior. Consider a droplet of fluid with density ρ, surface tension γ, and dynamic viscosity μ deposited on substrate which provides high droplet mobility. The droplet reaches a somewhat flattened equilibrium shape under the influence of terrestrial gravitational acceleration g_0. If the system is exposed to a step reduction in gravity, the flattened droplet will reorient producing a force normal to the substrate surface. In this scenario, droplet jump from the substrate may occur as a droplet of radius R traveling with velocity v. This droplet jump process can be characterized by three dimensionless groups: Bond number $Bo_0 = \rho g_0 R^2/\gamma$, Weber number $We = \rho R v^2/\gamma$, and Ohnesorge Number $Oh = \mu/\sqrt{\rho\gamma R}$.

Jha et al. [1] developed a model for the rebound of viscous droplets from a superhydrophobic surface which showed good agreement with experiments. Here, this model is revisited to account for new initial conditions to predict the velocity of a droplet jump. The model considers the droplet as a spring-mass-damper system, with each component associated with surface tension, droplet mass, and viscosity, respectively.

4.2 Methods

The particle beds are constructed with either polyethylene or polystyrene polydispersed spheres with diameters in the ranges 125-150 μm and 600-1000 μm, respec-

tively. The particle bed is created by depositing a thin layer of particles on a slightly concave 50 mm diameter glass substrate. For the larger particles, the bed consists of a single layer of particles. For the smaller particles, a mound of particles is deposited in the middle of the concave lens and spread by compressing the mound with a convex lens of the same curvature until the particles have spread to a layer $\lessapprox 10$ particles thick . The glass substrate is cleaned with ethanol before every test. Compared to previous studies with deep particle beds [62, 68, 67, 69, 70, 66, 65, 63, 64], the thin layer of particles on top of the rigid glass substrate provides minimal compliance during the droplet jump. The liquids used to form droplets consist of water-glycerol mixtures with viscosity 1-1410 mPa·s and surface tension 63-72 mN·m^{-1}. Drop volumes are 0.2-2.0 ml. The fluid is delicately deposited on the particle bed before each test using a syringe. Note that if done carelessly, the liquid would push the particles aside, touch the hydrophilic base substrate, and spread on the base substrate displacing the particles and creating a puddle.

These experimental conditions allow to explore the problem in the following parameter ranges: Bo_0 1.8-8.6, We 0.05-1.40, and Oh 0.001-1.900. Note that, these experiments include jumps up to $Oh = 1.9$, over twice the parameter range of previous studies [1, 58, 48, 59].

All experiments are performed at the Dryden Drop Tower (DDT) facility at Portland State University. The DDT is a safe, low-cost, high-rate facility located in the atrium of an engineering building on campus. The experimental apparatus is mounted to an aluminum chassis, or 'drop rig', which hangs inside the DDT drag shield before each drop. During a drop, the rig and drag shield are released

simultaneously and do not make contact throughout the microgravity period of the drop; note that because the rig is enclosed in the drag shield, it is largely protected from aerodynamic drag during free fall. The drag shield and experiment rig fall 22 m providing 2.1 s of high quality low-gravity g $< 10^{-4} g_0$. Additional information can be found in Wollman [71].

Experiments are imaged at 60 fps using a consumer-grade camera (Panasonic, HC-WX970) or, when faster acquisition was needed, 300 fps using a high speed camera (Kron Technologies, Chronos 2.1-HD). A diffuse LED array is adopted to backlight the phenomena, as it has been done extensively by our group [61, 72]. Images from a typical Drop Tower test are shown in Fig. 4.1. Finally, droplet positions are determined by fitting an ellipse to the droplet and recording the centroid position using image analysis software Fiji [46]. Maximum uncertainty for the velocity is 0.03 cm/s.

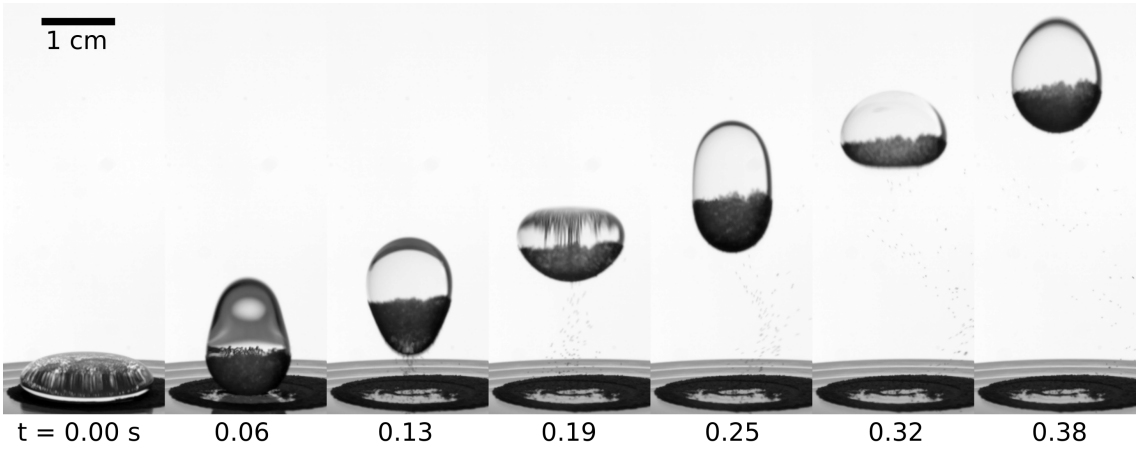

Figure 4.1: Montage from a drop tower test showing a 1.0 ml droplet jumping from a bed of 125-150 μm polyethylene particles. A circular region of clean glass where the particles have been carried away by the droplet is clearly visible. Particles which have detached from the droplet are visible after the third frame.

4.3 Model

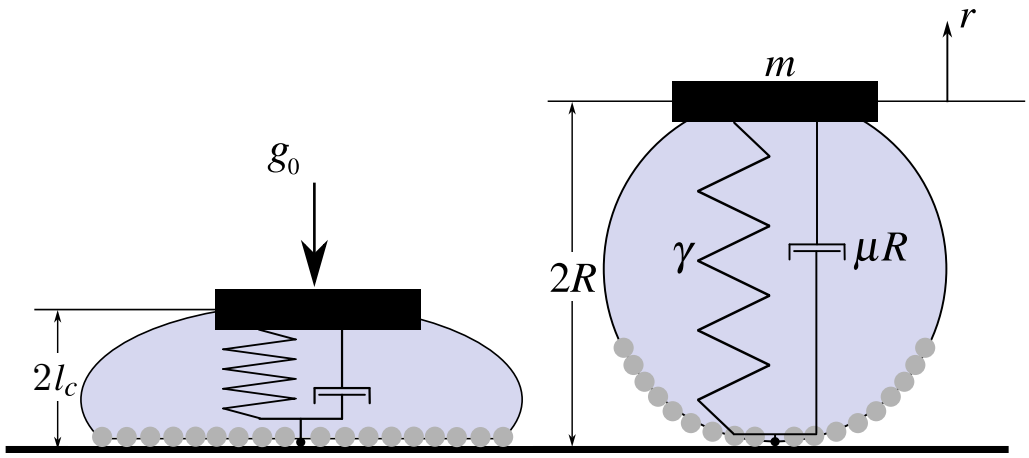

Figure 4.2: Diagram depicting how the droplet is modeled as a spring-mass-damper system with stiffness γ, damping μR, mass m, and free length $2R$. Left: the initial condition of the droplet under terrestrial gravitational acceleration g_0 with height $2l_c$. Right: droplet in a spherical geometry so the spring is uncompressed ($r = x = 0$).

The droplet jump is modeled as a mass-spring-damper system. A diagram of the system considered is provided in Fig. 4.2. The mass is taken as the droplet mass, neglecting any attached particle mass. and the spring constant is assumed as the surface tension of the fluid, γ. A scaling argument for the viscous dissipation denoted as $F_v = (\mu\frac{u}{R})R^2$ [1]. Therefore, the damping coefficient is μR. The free length of the 'spring' is $2R$. The equation of motion can then be written as:

$$m\ddot{r} + \mu R\dot{r} + \gamma r = 0, \tag{4.1}$$

where r designates drop deformation and dot(s) derivative(s) with respect to time.

For the relatively large fluid volumes studied here, the initial gravitational accel-

eration, g_0 =9.81 m/s^2, induces a body force that is significant compared to surface tensions as revealed by Bond numbers $Bo_0 = (R/l_c)^2 > 1$, where l_c is the capillary length $l_c = \sqrt{\gamma/(\Delta\rho g)}$ and $\Delta\rho$ is the density difference between the liquid and gas phase. As a result of the balance between gravity and surface tension, the droplets adopt a puddle or disk shape with a height of $2l_c$ when deposited onto the particle bed. Therefore, the initial condition for drop deformation is $r = -2(R - l_c)$. The second initial condition is $\dot{r} = 0$ as the drop initially being completely static without any internal flow, which may not be the case for a rebounding droplet [60].

Equation (4.1) is non-dimensionalized by scaling the length by the drop radius R, and the time by the inertio-capillary time scale $t_0 \equiv (m/\gamma)^{1/2}$ yielding:

$$\ddot{x} + \mathrm{Oh}\dot{x} + x = 0, \tag{4.2}$$

where $x \equiv r/R$ is the dimensionless deformation. The initial conditions become $x = (4/Bo_0)^{1/2} - 2$ and $\dot{x} = 0$. It is noted that with this non-dimensionalization $\dot{x} \equiv We$. The solutions to eqn (4.2) for $x(Oh, Bo_0)$ and $\dot{x}(Oh, Bo_0)$ are the product of exponentially decaying sine and cosine functions.

4.4 Results

One interpretation of the solution to eqn 4.2 is that the droplet detaches from the surface when the spring reaches its free length. Such an interpretation would lead

to a jump time of a quarter cycle or:

$$\tau_{x=0} = \frac{\pi}{\sqrt{4 - Oh^2}}. \tag{4.3}$$

Performing a series expansion of Eq. 4.3 yields $\tau_{x=0} \approx \frac{1}{2} + \frac{1}{16} Oh^2$. Taking the pre-factor of Oh^2 as a free parameter, the experimental data can be fitted to the equation resulting in a jump time:

$$\tau_j = \frac{1}{2} + \frac{1}{2} Oh^2. \tag{4.4}$$

This equation is plotted in Fig. 4.3 along with the experimental data. This equation is exactly one half the rebound time found by Jha et al. [1]. Such a result is expected since the experiments presented here do not include the spreading phase of droplet rebound. Notably, no additional dissipation is being introduced by the presence of the particle raft.

The droplet morphology at the jump time provides insight to the error in the the prediction of eqn 4.4. The error in the model can be explained by considering the droplet morphology and the moment of jumping compared to the model assumption of a spherical droplet. With reference to Fig. 4.4, it is shown that for droplets with small Oh the droplet leaves the substrate as a prolate droplet. This larger droplet extension before leaving the substrate explains the larger jump time compared to the model. Furthermore, as Oh is increased there is a transition in morphology from a prolate droplet to an oblate droplet. In particular, at $Oh \sim 1.0$, Fig. 4.4 shows a oblate drop jump, such a jump is accompanied by an over-prediction of

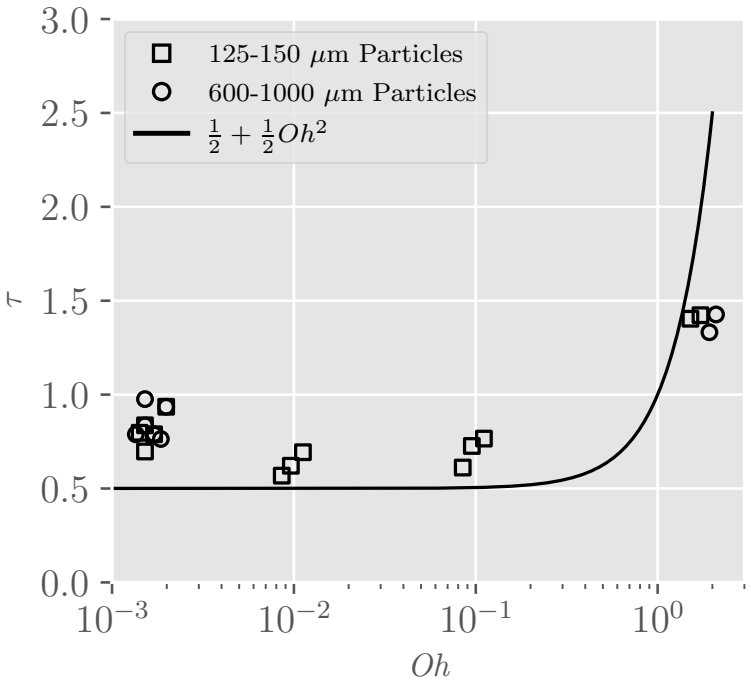

Figure 4.3: Experimental data for non-dimensional jump time compared against $\tau_{x=0}$ from eqn (4.4).

the jump time. At these large viscosities, droplet mobility can be reduced even on superhydrophobic substrates due to sticking/pinning of the liquid on the substrate [8]. The details of the droplet morphology are not captured by the presented model, but these observations suggest valuable future work.

A prediction for the Weber number is evaluated as $\dot{x}(\tau_{x=0})$. A comparison between the predicted Weber number and the measured Weber number is presented in Fig. 4.5. Overall, droplet jumps from particle beds tend to exhibit Weber numbers closer to the predicted Weber number. A comparison between the predicted Weber number and the measured Weber number, including data for Oh and Bo,

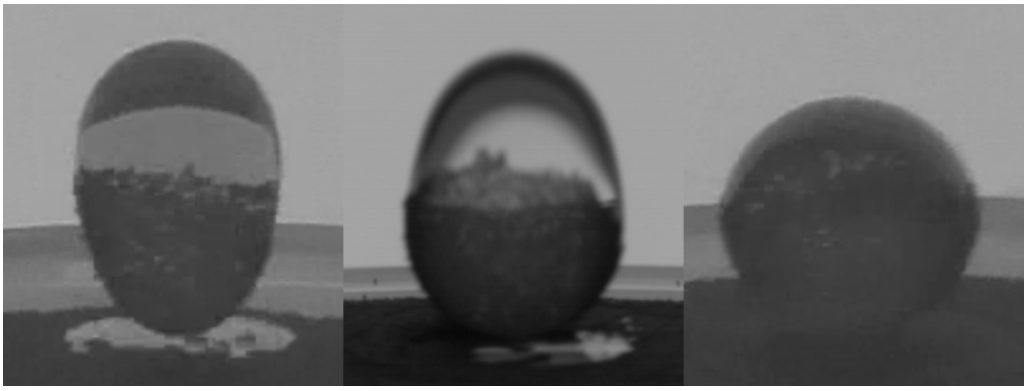

Figure 4.4: Images from Drop Tower tests showing the moment the droplet detaches from the substrate for $Oh \sim 0.001, 0.1, 1.0$ increasing from left to right.

is presented in Fig. 4.6 Agreement is shown across the full parameter range. It is shown that experimental Weber numbers approach zero near the critical value of $Oh = 2$ where the system becomes overdamped and viscosity is expected to suppress jumping. The model shows a shift from slight We over-prediction for $Bo_0 < 5$ to a slight under-prediction for $Bo_0 > 5$. Additionally, droplet jump Weber numbers are slightly smaller for jumps from the larger particles.

The data from Attari et al. [7] and Juboori [8] is included for reference in Fig. 4.6. For water droplets, $Oh \approx 10^{-3}$, jump from a particle bed shows similar behavior to water jump from a superhydrophobic surface with resulting jump Weber number range of 0.4-1.4. When considering more viscous fluids, the data of Juboori [8] shows that drop jump velocities decrease above $Oh \approx 10^{-2}$. The data for droplet jump from a particle bed shows consistently higher jump velocities that jump from a superhydrophobic surface. Additionally, a less steep decrease in jump velocities in response to increasing fluid viscosity is observed. Contact line dissipation and stick-slip behaviors of viscous aqueous glycerol solutions significantly decrease the

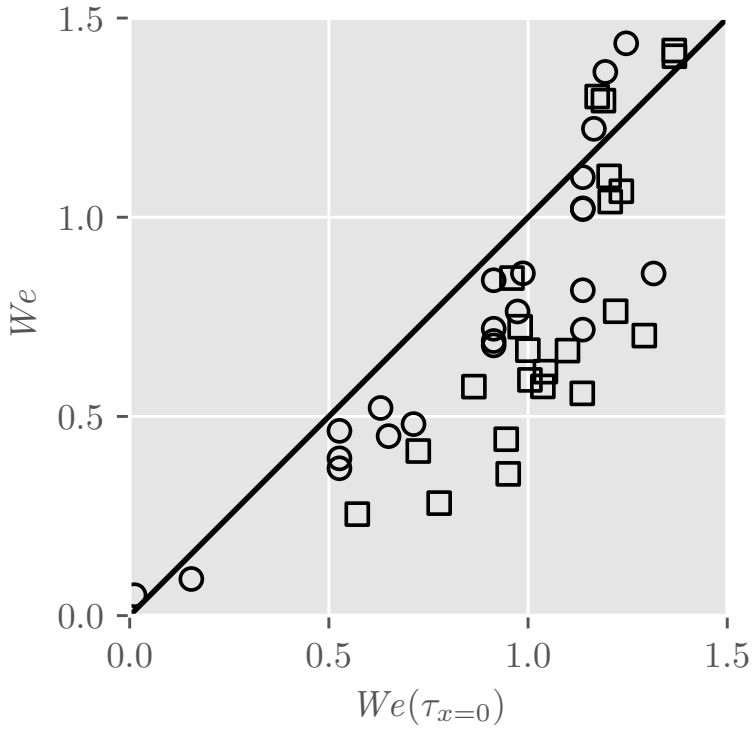

Figure 4.5: Drop tower data for jump Weber number compared against the predictive model. Circles correspond to droplet jump from a particle bed and square markers correspond to droplet jump from a superhydrophobic surface[7, 8].

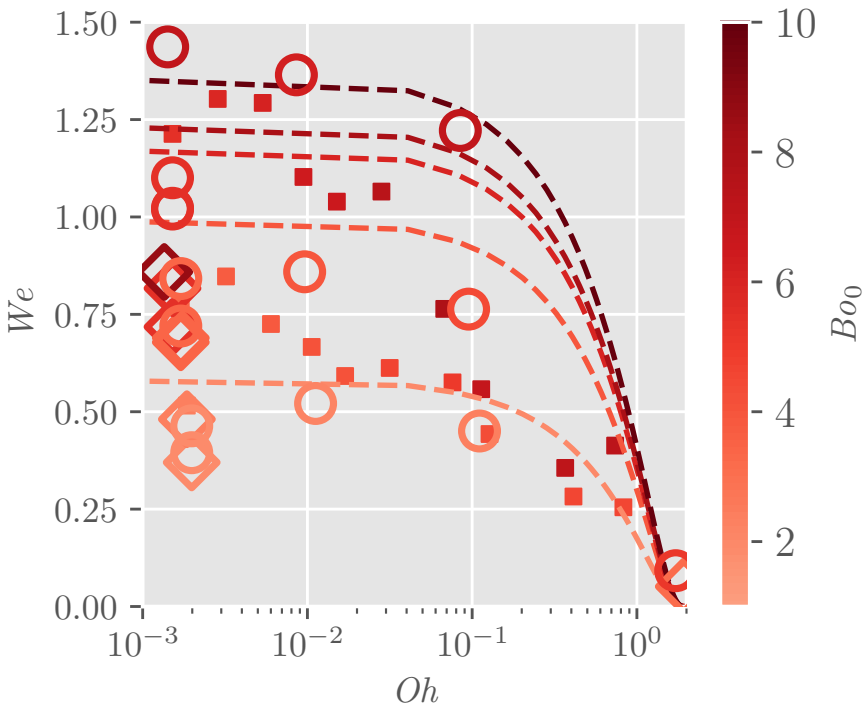

Figure 4.6: Drop tower data for jump Weber number compared against the predictive model. Hollow markers are experimental data for droplet jump from a particle bed. Circles and diamond markers correspond to $d_p = 125 - 150$ μm and 600-1000 μm, respectively. Square markers are experimental data from Attari et al. [7], Juboori [8] for droplet jump from a superhydrophobic surface. Lines are solutions to $We(\tau_{x=0})$ for $Bo_0 = 2, 4, 6, 8, 10$ to assist visual inspection.

dewetting velocity of a droplet, even in superhydrophobic surfaces. This investigation undoubtedly shows that when a droplet jumps from a particle bed, dewetting is no longer required and these sources of dissipation are avoided. It is also interesting to note that the presence of the particle raft does not impede this energy transfer.

The droplet surface area initially resting on the particles increases with droplet volume because the puddles have an approximately constant height, $H = 2l_c$. For a given area in contact with the particle bed, the mass carried away by the droplet when the jump occurs is greater for larger diameter particles. As expected, the partially wetting particles remain largely in a particle raft as the droplet travels away from the substrate, see Fig. 4.1. The raft does not significantly alter the geometry of the oscillating droplet as it travels away from the substrate. Further study into a greater range of particle wettability would be interesting but is beyond the scope of this work.

4.5 Conclusion

The first investigation of droplet jump from a particle bed has been presented. This study sheds light on the accuracy of the spring-mass-damper model of droplet jump for a wide range of fluid viscosities. The presence of the particle layer is shown to effectively remove contact line dissipation while not introducing any significant additional forms of dissipation. The effect of the Ohnesorge number on the morphology of the jumping droplet is identified. In addition to the larger viscosity range, the results match the model of Jha et al. [1] even for the unique initial conditions for

the droplets in this study.

Chapter 5

Cavity Collapse

5.1 Introduction

The collapse of a cavity has been studied over a large variety of cavity formation processes, see Fig. 5.1. The investigation of collapsing spherical cavities has received

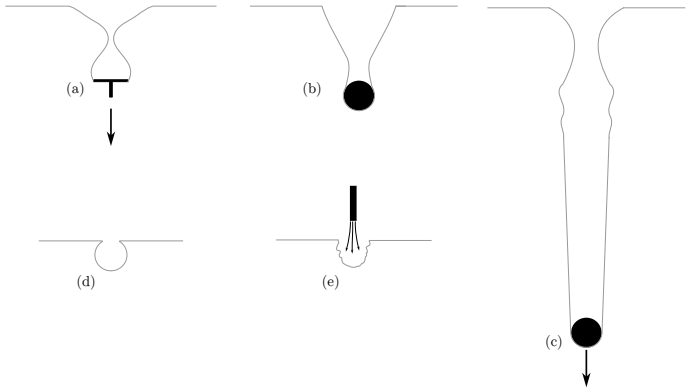

Figure 5.1: Illustrations of different methods to produce a cavity: (a) disk draw through a surface, (b) impact of a buoyant sphere, (c) impact of a hydrophobic steel sphere, (d) bubble collapse at a free surface, (e) cavity formed by an impinging air jet.

significant attention due to a wide range of applications from the effervescence of champagne [73] to role of breaking waves in the regulation of ocean–atmosphere

interactions [74, 73]. Such studies are focused on bubbles bursting at a free surface, fig. 5.1(a). After a bubble bursts, capillary waves collide at the bottom of the cavity forming a liquid jet from which drops detach and are emitted to the surrounding atmosphere. Duchemin et al. [75] presented the first DNS of the axisymmetric bubble bursting by solving for the two-phase Navier–Stokes equations and demonstrated that the main controlling parameter of the speed and size of the first ejected droplet is the Laplace (or Ohnesorge number. These simulations showed that there is an optimal Laplace number around 1,000 that leads to the generation of a very fast thin jet. The optimal Laplace number corresponds to the most effective focusing, with shorter (and slower) capillary waves damped by viscosity, so that the fastest capillary waves collide and give rise the jet. The a thin high-velocity jet is formed at the boundary of bubble entrapment regime where a small dimple forms at the base of the cavity and a bubble is trapped in the bulk fluid below the base of the jet. The cavity geometry was shown to evolve according to $(t_c - t)^{2/3}$, where t_c is the collapse time.

Significant work has been performed linking the bursting dynamics with the physical properties of the liquid. Ghabache and Séon [76] developed scaling laws for the liquid jet velocity. Gañán-Calvo [77] developed scaling laws for the jet velocity, as well as the radial and axial length, as a function of the liquid properties. The effects of gravity have been investigated theoretically and numerically [78, 79].

Zeff et al. [80] investigated the collapse of cavities generated from standing waves in a cylindrical container. The waves were generated by Faraday excitation. A critical standing wave height was observed which entrapped a bubble and generated

a slender high speed jet. It was shown that the liquid-water interface, before the surface wave collapses at time t_c, is self-similar and obeys a $(t_c - t)^{2/3}$ inertial-capillary scaling law.

Ghabache et al. [81] investigated the jet generated from the gravity driven relaxation of a cavity formed by the impact of an air jet and a free surface, fig. 5.1(b). This investigation included a maximum cavity aspect ratio of $H/R \sim 2$. A model was developed which captures the dependence of the jet velocity on gravitational acceleration and geometry (height and width) of the cavity. Benusiglio et al. [82] investigate the collapse of cavities generated by the explosion of a firecracker near the free surface.

Cavities generated from the collision of a solid body have also been studied. Aristoff et al. [83], Aristoff and Bush [84] investigated the impact of a hydrophobic sphere at low bond numbers, fig. 5.1(c). Four regimes were identified, quasi-static, shallow seal, deep seal and surface seal, and show to depend on Froude number, Weber number, and Bond number. The wetting properties of the impacting sphere were important to the cavity dynamics.

Most studies of such cavities generated from an impacting solid body have been in the gravitational regime $Bo >> 1$ and the cavities tend to have high aspect ratios. Examples are cavities generated by pulling a body through a free surface, fig. 5.1(a,b), or impact solid body dropped from above the liquid bath [85–88]. Aristoff et al. [3] limited the depth of the cavity by using a buoyant body for impact, fig. 5.1(d). In this case, the base of the cavity is still constrained to the shape of the solid body and the collapse is still gravity driven.

The evolution of an initially stationary axisymmetric air cavity depends only on six physical parameters: the radius R, the height H, the dynamic viscosity μ, the surface tension γ, the density ρ, and the acceleration due to gravity g. The initial geometry is characterized by the aspect ratio R/H. Two length scales can be constructed

$$l_c = \sqrt{\frac{\gamma}{\rho g}} \tag{5.1}$$

and

$$l_\mu = \frac{\mu^2}{\rho\gamma}. \tag{5.2}$$

For water in a terrestrial environment, with g_0 =9.81 m s^{-2}, l_c =2.7 mm and l_μ =0.014 µm. Two additional dimensionless numbers characterize the problem - the Bond number

$$Bo \equiv \frac{R}{l_c} = \frac{\rho g R^2}{\gamma} \tag{5.3}$$

(relative importance of gravitational forces compared to surface tension forces) and the Laplace number

$$La \equiv \frac{R}{l_\mu} = \frac{\rho\gamma R}{\mu^2} \tag{5.4}$$

or Ohnesorge number

$$Oh \equiv \frac{1}{\sqrt{La}} \tag{5.5}$$

(relative importance of surface tension forces to viscous forces).

This work presents a novel investigation of the pure capillary collapse of a large,

$Bo_0 \equiv \rho g_0 R^2/\gamma > 1$, cavity. The influence of the initial shape of the cavity on the characteristics of the resulting liquid jet are studied. The evolution of the cavity shape is also investigated.

5.2 Methods

5.2.1 Drop tower experiments

A schematic of the experiment is provided in Fig. 5.2. Before each test a fixed volume of air is added to the pressure vessel. The velocity of the jet can be varied by adjusting the volume of air added to the pressure vessel. A micro controller in combination with an accelerometer are used to actuate the solenoid valve open in response the step reduction in gravity at the start of the drop tower test. The air jet impinges the water surface forming an elongated cavity. After the cavity if formed, the solenoid is closed to stop the air flow and the cavity collapses process ensues. The open time of the solenoid valve was between 50-100 ms for all tests. At the end of the drop tower test, after free fall, residual pressure in the system was released by actuating the valve open so that the pressure vessel reached atmospheric pressure.

The nozzle was an 8 gauge stainless dispensing needle with an inner diameter of 3.43 mm. The nozzle could be translated vertically to adjust the distance between the nozzle exit and the water surface. By tuning these three parameters (jet intensity, jet duration, and nozzle height) a variety of cavity aspect ratios may be achieved.

A clear cylindrical fluid tank with diameter 100 mm was used. Water with density

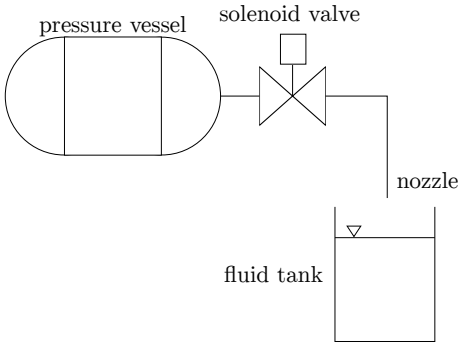

Figure 5.2: Diagram showing the flow components used to generate the cavity during the drop tower test.

$1000\,\mathrm{kg\,m^{-3}}$, viscosity $1\,\mathrm{mPa\,s}$, an surface tension $72\,\mathrm{mN\,m^{-1}}$ is used as the working fluid. To decrease optical distortion, the cylindrical tank was placed inside a square tank and the gap between the two tanks was filled with the working fluid. The liquid tank was large enough so that the waves generate by the cavity collapse did not interact with the walls of the container before the cavity collapse had occurred. Cavity aspect ratios up to $H/R = 4.5$ were achieved.

The experiment is backlit with a diffuse led panel. Images are captured at 1000-2500 f.p.s. using a high speed camera (Chronos 2.1-HD). The spatial resolution was $47\,\mu\mathrm{m}$ per pixel. The height and width of the cavity were measured at their maximum values. Jet drop positions were measured by fitting an ellipse to the droplet and taking the centroid of the ellipse as the drop centroid. Image analysis was performed using ImageJ software [46].

5.2.2 Simulations

Direct numerical simulations are employed to study the cavity collapse. The free software Basilisk [18, 19] is used to solve the Two-dimensional axisymmetric, incompressible two-phase Navier-Stokes equations with surface tension. The collapse of cavity of radius R, gas density ρ_{gas}, and dynamic viscosity μ_{gas} surrounded by liquid of density ρ_{liq}, dynamic viscosity μ_{liq}, and surface tension γ is considered, Fig. 5.3. From these parameters three dimensionless groups are constructed which describe the phenomena: the density ratio $\rho_{\text{ratio}} = \rho_{\text{gas}}/\rho_{\text{liq}}$, viscosity ratio $\mu_{\text{ratio}} = \mu_{\text{gas}}/\mu_{\text{liq}}$, and the Laplace number

$$La \equiv \frac{\rho_{\text{liq}}\gamma R}{\mu_{\text{liq}}^2}. \tag{5.6}$$

All lengths are non-dimensionalised by the cavity radius R. The velocity field and time are non-dimensionalised with the inertio-capillary velocity,

$$v_\gamma = \sqrt{\frac{\gamma}{\rho_{\text{liq}} R}}, \tag{5.7}$$

and time,

$$t_c = \sqrt{\frac{\rho_{\text{liq}} R^3}{\gamma}}, \tag{5.8}$$

respectively. The pressure is non-dimensionalised with the capillary pressure, $p_\gamma = \gamma/R$. The resulting incompressible two-phase Navier-Stokes equations with surface tension can be written in the classical one-fluid formulation [89]:

$$\frac{\partial \bar{\mathbf{u}}}{\partial \bar{t}} + \bar{\nabla} \cdot (\bar{\mathbf{u}} \otimes \bar{\mathbf{u}}) = \frac{1}{\bar{\rho}} \left[-\bar{\nabla}\bar{p} + \frac{1}{\sqrt{La}} \bar{\mu} \bar{\nabla} \cdot \left(\bar{\nabla}\bar{\mathbf{u}} + \left(\bar{\nabla}\bar{\mathbf{u}} \right)^T \right) + \bar{\kappa}\bar{\delta}_s \mathbf{n} \right] \tag{5.9}$$

$$\frac{\partial c}{\partial \bar{t}} + \bar{\mathbf{u}} \cdot \bar{\nabla} c = 0 \tag{5.10}$$

$$\bar{\nabla}\bar{\mathbf{u}} = 0 \tag{5.11}$$

Where to dimensionless density and viscosity are:

$$\bar{\rho} = c + (1 - c)\rho_{\text{ratio}} \tag{5.12}$$

$$\bar{\mu} = c + (1 - c)\mu_{\text{ratio}}. \tag{5.13}$$

Here c is the VoF tracer

$$c = \begin{cases} 1 \text{ in the liquid} \\ \\ 0 \text{ in the liquid} \end{cases} \tag{5.14}$$

The domain size is is a square sized $15R \times 15R$. The maximum resolution was $2^{14} \times 2^{14}$ cells with 1092 grid points across the cavity radius. The free surface of the fluid surrounding the void is in the middle of the domain. The edge where the flat free surface meets the cavity is smoothed with a radius of $0.1R$.

Throughout the simulation the number, size, and velocity of droplets generated from the collapse are tracked. Additionally, the cavity profiles are exported through

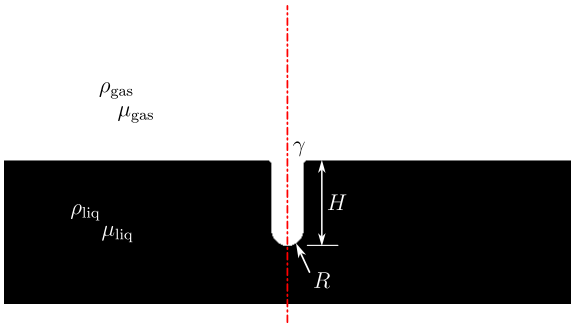

Figure 5.3: Simulation domain and relevant parameters. Total domain size is $15R \times 15R$. The dashed red line represents the rotational axis.

the simulation. The adaptive mesh refinement allows the code to efficiently resolve the different scales of the problem. Despite a maximum resolution of 4^{14} cells, the simulation takes only $\sim$48 hours running on 8 cores.

5.3 Results

Cavities with aspect ratios up to H/R=4.5 we generated in drop tower tests. For aspect ratios $H/R < 3.7$ no jet was generated from the cavity collapse. The temporal development of the collapse of two different cavities is displayed in Fig. 5.4. In the more shallow cavity of Fig. 5.4(a), $H/R = 3.7$, the collapse of the cavity rims is subdued by interactions with the bottom of the cavity with the collapsing walls. The collapse generates a large droplet $R/R_d = 0.3$ with velocity $0.3\,\mathrm{m\,s^{-1}}$. Figure 5.4(b) shows the collpase of a higher aspect ratio cavity, H/R=3.9, generating a more slender jet with first jet drop $R/R_d = 0.2$ and velocity $1.7\,\mathrm{m\,s^{-1}}$. In this case, multiple droplets are generated in contrast to the single jet drop is the test shown in Fig. 5.4(a). Figure 5.5 shows a the collapse of a cavity with $H/R = 4.5$ which

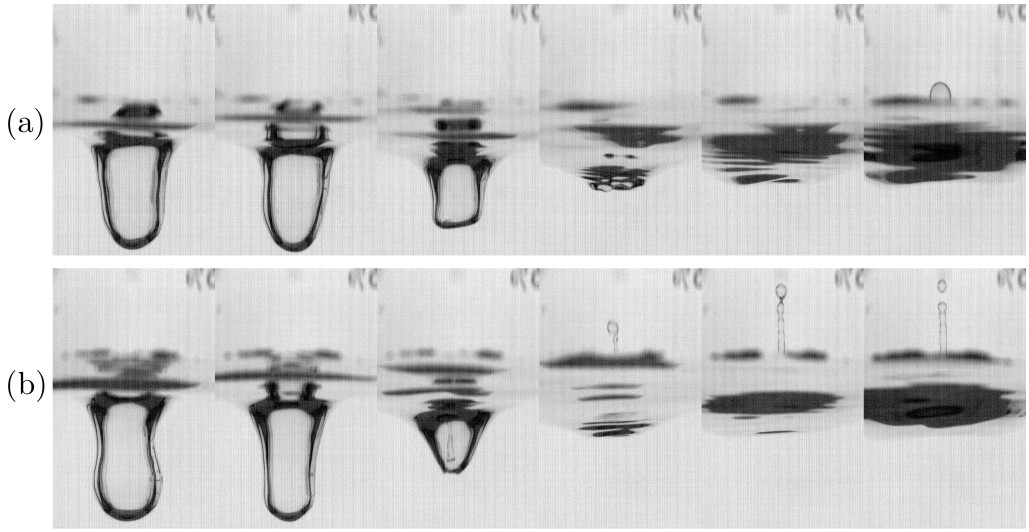

Figure 5.4: Image montages showing the microgravity collapse of two different air cavities in water. H/R= 3.7 and 3.9 for (a) and (b), respectively. .

leads to an extremely thin and fast jet. Additionally, a bubble being trapped along the cavity axis is observed. The droplet size is $R/R_d = 0.04$ and the velocity is v =5.0 m s^{-1}. For this drop the initial jet droplets are barely visible at the 2,500 f.p.s recording speed, and it is likely that the velocity is measured for a drop which is not the fastest drop.

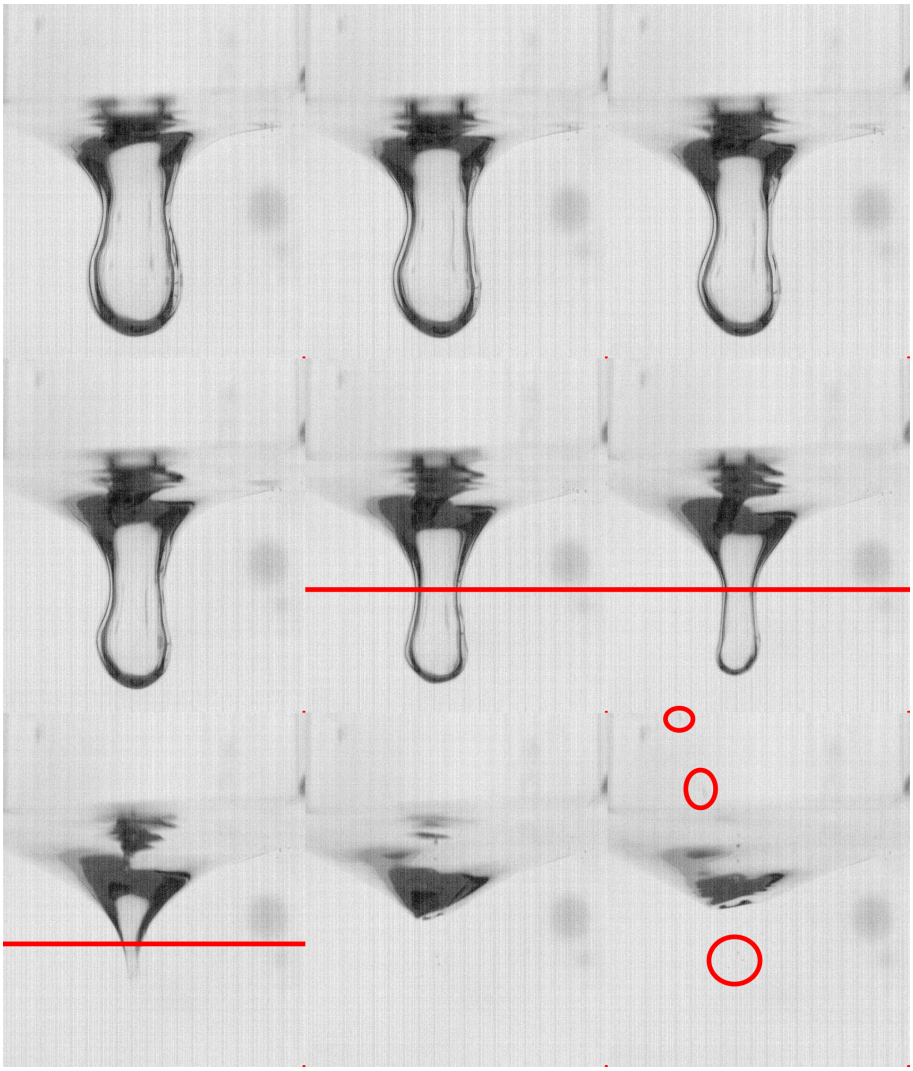

Figure 5.5: Images from drop tower test showing a jet emerging from the base of the cavity before the walls of the cavity collapse. Initial cavity aspect ratio $H/R = 4.5$. The minimum radius of the cavity primary wall is indicated by a line. Jet droplets and trapped bubble are circled in red. Frames are 2.4 ms apart.

To further investigate the apparent jet behavior, a parametric numerical study of the cavity aspect ratio $H/R = 4.2 - 4.7$ was performed. The relevant dimensionless groups for the simulation were taken as $\rho_{\text{ratio}} = 1/998$, $\mu_{\text{ratio}} = 1/55$, and and $La = 10,000$. Simulations show a similar dependence of the jet velocity on the aspect ratio of the cavity. Figure 5.6 shows an abrupt increase in the velocity of the top jet drop for an aspect ratio of 4.5. A maximum value of $Ca \sim 50$ is observed. The magnitude of this peak is similar to previous studies [75, 79]. This peak in velocity coincides with the boundary of bubble entrapment regime.

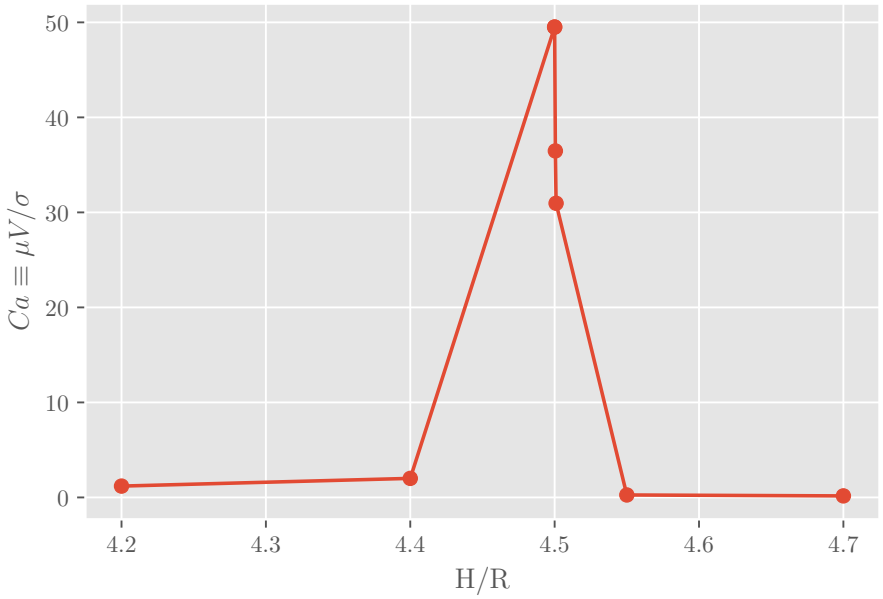

Figure 5.6: Capillary number of the jet top droplet for H/R 4.2-4.7 and $La = 10,000$. At $H/R = 4.5$ an abrupt increase in drop velocity coincides with the initial trapping of a bubble.

Figure 5.7 show the cavity profile just after collapse for $H/R = 4.5$ and 4.55. It in clear that the jet emerges before the collapse of the cavity walls. It is shown

that the maximum jet velocity occurs and the threshold of bubble entrapment. For aspect ratios greater than 4.5 the collapse occurs at the same height.

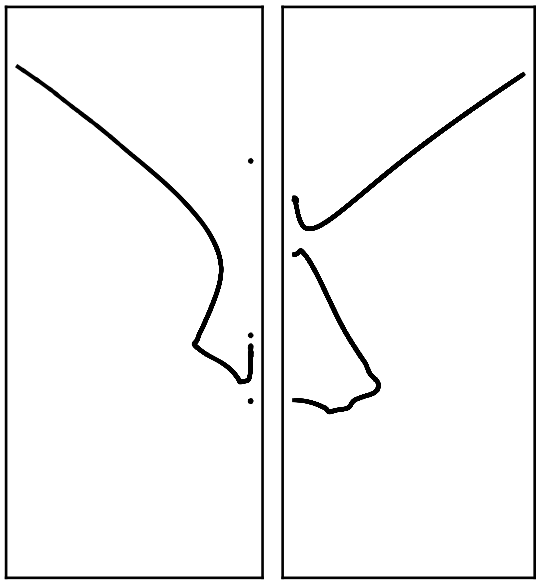

Figure 5.7: (left) Cavity profile for H/R = 4.5 and (Right) Cavity profile for H/R = 4.55 at $t/t_c = 0.96$.

Simulations are performed for a cavity with H/R=4.5 and cavity profiles are exported every 0.04 ms. Cavity profiles are shown in Fig. 5.9(a). The minimum radius of the cavity wall is identified and tracked through time. The points are found to evolve according to $(t_c - t)^{0.546}$. This is consistent with previous experimental and numerical studies [90–92]. R^2_{min} is plotted in Fig. 5.9(b). The data can be extrapolated to determine t_c = 40.19 ms. Cavity profiles scaled by $(t_c - t)^{1/2}$ are presented in Fig. 5.9(c). The scaled profiles are shifted vertically so that the cusp of the cavity is aligned through time. While the radius of the cavity wall follows $(t_c - t)^{1/2}$ the overall shaped of the cavity is not self similar through the time range

considered. This is especially apparent at the bottom of the cavity, fig. 5.9(c). The curvature at the bottom of the cavity is initially concave and switches to convex as the cavity collapses. The relatively fast motion of the base of the cavity relative to the walls creates a notch, fig. 5.9(a). For aspect ratios $H/R > 4.5$ the notch contributes to the volume of the trapped bubble.

The cavity profiles are extracted from images captured during drop tower tests. Figure 5.8(left) shows the experimental cavity profiles. Figure 5.8 (right) shows the experimental cavity profiles scaled according to $(t_c - t)^{1/2}$. In this case t_c is determined by fitting two rescaled profiles over each other. The camera resolution prevents capturing profiles closer to the collapse time.

Figure 5.8: Cavity profiles extracted from drop tower experiment (left) and scaled by $(t_c - t)^{1/2}$ (right).

The profiles shortly after the initial generation of the jet are shown in Fig. 5.7. It is shown the that a small change in the aspect ratio of the cavity can drastically change the volume of the entrapped bubble. It is also shown that the the jet is

generated before the collapse of the cavity wall.

Additional simulations are performed where the cavity profiles are exported with better temporal resolution near the collapse time. Profiles are exported every 0.04 ms. Near the collapse time a dimple forms at the base of the cavity. It is shown in Fig. 5.10(a) that the walls of the dimple are traveling faster the the cavity walls. The base of the dimple is relatively stationary compared to its walls. The cusp of the dimple is tracked through time. Fig. 5.10(b) shows the walls at the base of cavity evolve at $R \sim (t_c' - t)^{2/3}$, where $t_c' = 40.07$ ms is a new collapse time for the base of the cavity. Profiles scaled according to $(t_c' - t)^{2/3}$ are provided in Fig. 5.10(c). The collapse of this smaller cavity leading to a high speed slender jet is similar to the observation of Duchemin et al. [75] for the case of a bursting bubble. At aspect ratios greater than 4.5, the jet which emerges from the dimple jet is blocked by the closing of the larger cavity.

(a)

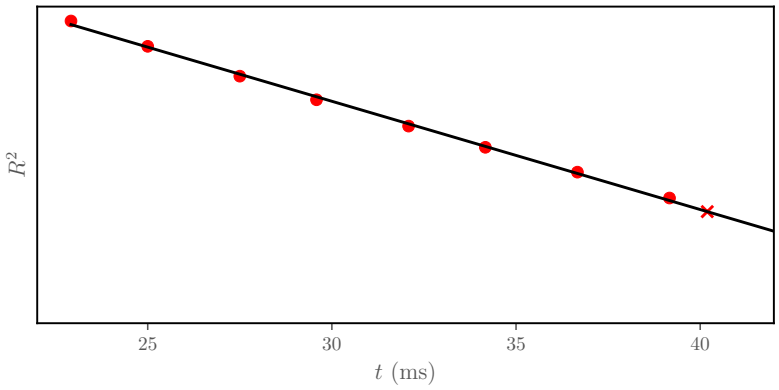

(b)

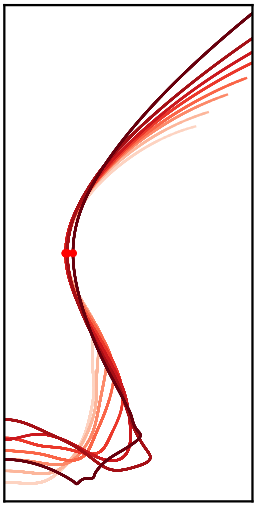

(c)

Figure 5.9: (a) Profiles extracted from simulation at times $t_c - t$=[17., 15., 13., 11., 8., 6., 4., 1.] ms. Red circles identify the cusp of the profile. (b) Red circles identify the cusp of the profile. R^2 is plotted against time. The collapse time is determined from the linear fit as $t_c = 40.19$ ms. The cusp radius is measured at $t_c - t$=[17., 15., 13., 11., 8., 6., 4., 1.] ms. (c) Profiles scaled by $(t_c - t)^{1/2}$ at times $t_c - t$=[17., 15., 13., 11., 8., 6., 4., 1.] ms. Red circles identify the cusp of the profile.

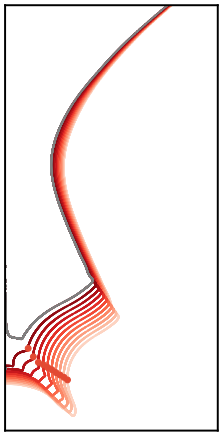

(a)

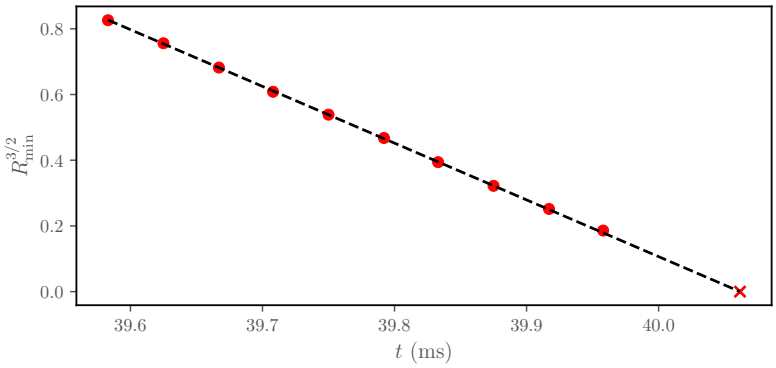

(b)

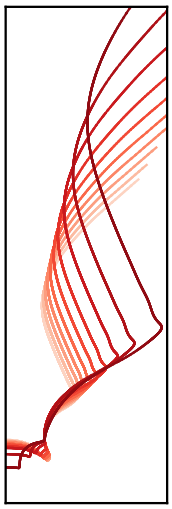

(c)

Figure 5.10: (a) Tracked points on at trough of cavity. (b) Red circles identify an minimum radius on the cusp region at the base of the cavity. $R^{3/2}$ is plotted against time. The collapse time is determined from the linear fit as $t_c' = 40.07$ ms. The cusp radius is measured at $t_c' - t$=[0.48, 0.44, 0.39, 0.35, 0.31, 0.27, 0.23, 0.19, 0.14, 0.10] ms. (c) Profiles scaled by $(t_c' - t)^{2/3}$ at times $t_c' - t$=[0.48, 0.44, 0.39, 0.35, 0.31, 0.27, 0.23, 0.19, 0.14, 0.10] ms. Minimum radius on the cusp region at the base of the cavity.

5.4 Conclusions

Slender cavities have been created in a microgravity environment by momentarily impinging a free liquid surface with an air jet. Drop tower experiments show the collapse of a high aspect ratio cavity can lead to jet formation. Holding the fluid properties constant, jets can generate huge slow moving droplets or very small high velocity droplets depending on the initial cavity geometry.

Previously Duchemin et al. [75] showed that singular jet behavior could be achieved from the same initial geometry of a bursting bubble by altering the Laplace number concluding the paper with the statement:

> *However other changes in the initial condition may cause a change in the position of the various singularities. In other words, for a given radius, it would be possible to reach a singularity by changing the shape of the bubble.*

Here it shown for the first time that singular jet behavior can be achieved by altering the initial geometry of the collapsing cavity.

A parametric study using simulations shows the dependence of the jet velocity on the initial cavity geometry. A critical aspect ratio of $H/R = 4.5$ is found where there is a sharp peak in the jet drop capillary number. This high speed jet emerges from a small dimple which collapses at the base of the cavity before the main walls of the cavity collide. Drop tower tests also show this abrupt increase in jet velocity near H/R=4.5. It is shown that the main cavity walls evolve with $(t_c - t)^{1/2}$ and the dimple walls evolve with $(t'_c - t)^{2/3}$ for the time ranges considered.

Chapter 6

Conclusions

6.1 Review of findings

The initial objective of this thesis was to better understand phenomena which may occur during a droplets lifetime, namely: droplet capture, droplet interaction and droplet generation. Three investigations have been presented which provide insight into these ubiquitous, in both terrestrial and microgravity settings, phenomena through a lens of capillary flow. Each investigation was accompanied by a drop tower test campaign. The main findings of each study are provided below.

In Chapter 3 the impact of a droplet on a fiber array was investigated. A method of accurately delivering a droplet to the center of a fiber array was developed. A drop tower test campaign was performed to investigate the droplet impact and capture across a wide range of impact conditions and fiber array geometries. A model was developed to describe the dynamics of the droplet from the time it entered the array to when it reached equilibrium. The model agreed with experimental results across a wide parameter range. Contact line dissipation was identified as the dominant force decelerating the droplet. Droplet equilibrium configurations were largely spherical

and the fibers showed little deformation at equilibrium. The droplet was shown to navigate to one side of the arrays of fibers oriented in a line.

In Chapter 4 an investigation of droplet jump from a particle bed was presented. It was shown that a water droplet can jump from particle beds with similar velocity to droplet jump from a superhydrophobic substrate. This indicates that the particle beds, and particle raft which is present on the jumping droplet, do not introduce significant new forms of dissipation to the droplet. For Viscous liquids, droplets jumped from the particle bed faster than from superhydrophobic substrates. The model of Jha et al. [1] for droplet rebound was extended to droplet jump. The model agreed with experimental data for jump velocity and jump time. Finally, a relationship between the jumping droplet morphology at different viscosities and the jump time measured from experiments was described.

In Chapter 5 an investigation of the capillary collapse of a high aspect ratio cavity was presented. It was shown that the collapse of such a cavity can give rise to a jet which breaks up into droplets. Drop tower tests show a trend of increasing jet velocity with increasing cavity aspect ratio. A particularly fast and thin jet was generated from the collapse of a cavity with an aspect ratio $H/R = 4.5$. Simulations were employed to perform a parametric study of the aspect ratio on the resulting jet. Simulations showed an abrupt peak is the jet velocity at $H/R = 4.5$. This high speed jet did not emerge from the collapse of the main cavity walls, but rather from the collapse of a small dimple formed at the base of the cavity. Both simulations and experiments show that the radius of the cavity walls evolves according to $(t_c - t)^{1/2}$, where t_c is the collapse time of the cavity walls. The walls of the dimple at the base

of the cavity evolves according to $(t_c' - t)^{2/3}$, where t_c' is the collapse time of the dimple.

Each of these studies has produced novel data for a set of phenomena which have persistently gleaned interest from the fluid mechanics community. 400 drop tower tests were performed for this work and provide the foundation of this data. Such tests allow the effects of gravity to be disentangled from other effects and can explore distinctive initial conditions. In this way, a unique description of the surface tension driven dynamics have been presented. Models have been developed and simulations performed which capture the experimental data. It is hoped that this novel contribution is useful for understanding or designing systems which generate, collect, manipulate, utilize, or interact with droplets.

6.2 Outlook

There are a number of unexplored phenomena relating to each of the three problems presented in this thesis which seem worthy of investigation. A few interesting avenues for future work are presented here.

The fibers used in the droplet capture study of Chapter 3 exhibited small deformations after the droplet reached its equilibrium configuration. Drop impact on arrays of flexible fibers which would show large deformations would be interesting future work. Such fibers could be constructed by casting an degased liquid oligomer solution in glass capillaries as was done in Van de Velde et al. [93]. Other fiber shapes could also be investigated. An exploratory drop tower test was performed

with thin rectangular beams instead of cylindrical fibers, images from this test are shown in Fig. 6.1. The beams and droplet show large deformations at equilibrium and droplet is captured at the free end of the beams.

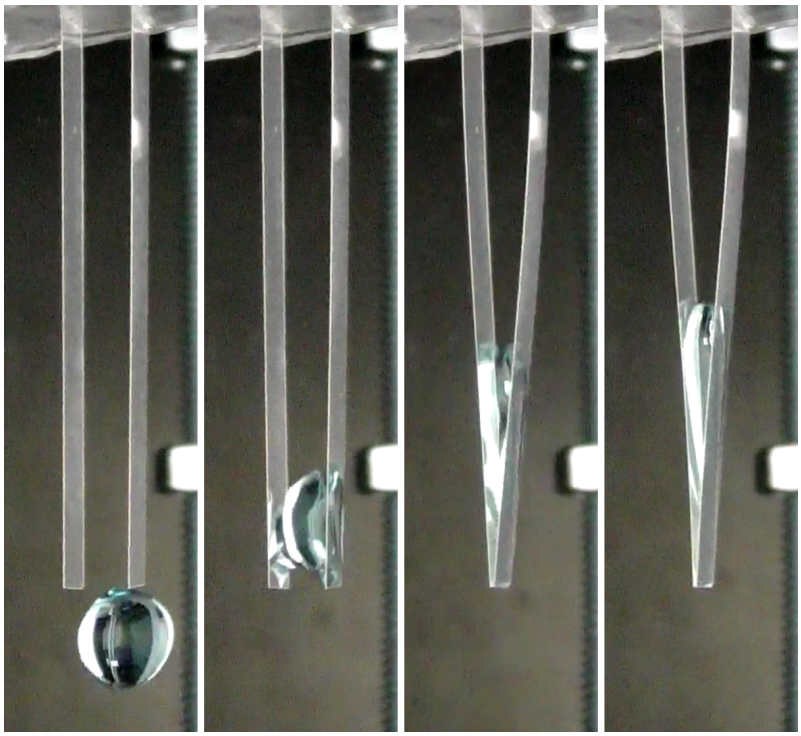

Figure 6.1: Images from drop tower test showing a droplet impacting two thin plastic beams.

The particle diameters used for the particle beds in the drop jump investigation of Chapter 4 were all very small compared to the radius of the droplet. It would be interesting to study droplet jump from beds of larger particles and characterize the role of particle size in the dynamics. Additionally, the jump of a droplet which is in contact, but not fully supported by, particles would be compelling. An exploratory drop tower test is presented in Fig. 6.2. Here a droplet is deposited on superhy-

drophobic surface and four large particles are placed around the droplet perimeter. When the droplet jumps, it carries the particles away with it.

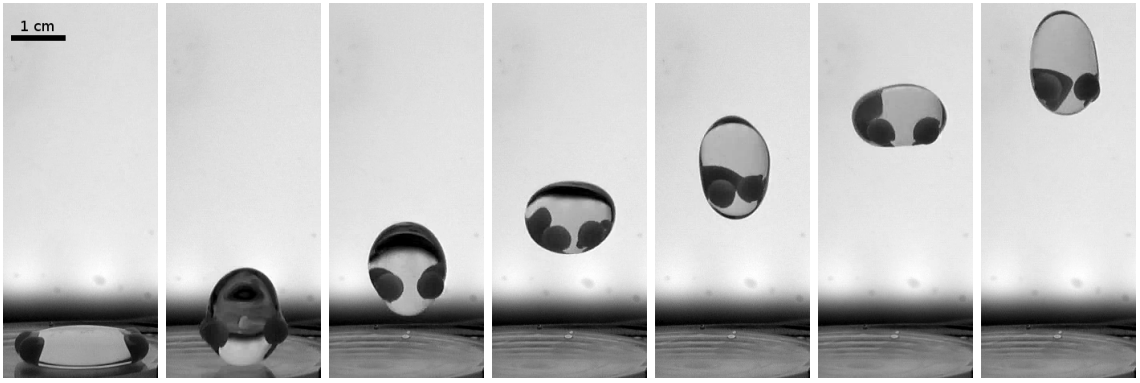

Figure 6.2: Images from drop tower test showing a 2ml water droplet carrying away four 5mm diameter nylon spheres as it jumps from a superhydrophobic surface.

An investigation of the collapse of a large cavity generated by impinging an air jet on a water surface in microgravity was presented in Chapter 5. Preliminary tests were performed with more viscous water-glycerol mixtures. These cavity generated in the water-glycerol mixture from the air pulse tended to be more conical compared to the relatively straight walled cavity formed in water. Looking further into the initial cavity geometry and resulting liquid jet dynamics would be of interest.

Bibliography

1 Aditya Jha, Pierre Chantelot, Christophe Clanet, and David Quéré. Viscous bouncing. *Soft Matter*, 16(31):7270–7273, 2020.

2 Runchen Zhao, Qianyun Zhang, Hendro Tjugito, and Xiang Cheng. Granular impact cratering by liquid drops: Understanding raindrop imprints through an analogy to asteroid strikes. *Proceedings of the National Academy of Sciences*, 112(2):342–347, 2014.

3 Jeffrey M. Aristoff, Tadd T. Truscott, Alexandra H. Techet, and John W. M. Bush. The water entry of decelerating spheres. *Physics of Fluids*, 22(3), 2010.

4 Andrew Paul Wollman. *Large Length Scale Capillary Fluidics: From Jumping-Bubbles to Drinking in SpaceBubbles to Drinking in Space*. PhD thesis, Portland State University, 2016.

5 Andrew Wollman and Mark Weislogel. New investigations in capillary fluidics using a drop tower. *Experiments in Fluids*, 54(4), 2013.

6 Karl Cardin, Sheng Wang, Olivier Desjardins, and Mark Weislogel. Rebound of large jets from superhydrophobic surfaces in low gravity. *Physical Review Fluids*, 6(1):014003, 2021.

7 B. Attari, M. Weislogel, A. Wollman, Y. Chen, and T. Snyder. Puddle jumping: Spontaneous ejection of large liquid droplets from hydrophobic surfaces during drop tower tests. *Physics of Fluids*, 28(10), 2016.

8 Taif Al Juboori. *The Effect of Viscosity on The Puddle Dynamics in Low Gravity Environment*. PhD thesis, Portland State University, 2021.

9 H. Lhuissier and E. Villermaux. Bursting bubble aerosols. *Journal of Fluid Mechanics*, 696:5–44, 2011.

10 Navajit Singh Baban, Sohini Saha, Sofija Jancheska, Inderjeet Singh, Sachin Khapli, Maksat Khobdabayev, Jongmin Kim, Sukanta Bhattacharjee, Yong-Ak Song, Krishnendu Chakrabarty, and Ramesh Karri. Material-level countermeasures for securing microfluidic biochips. *Lab on a Chip*, 23(19):4213–4231, 2023.

11 J. Plateau. I. experimental and theoretical researches on the figures of equilibrium of a liquid mass withdrawn from the action of gravity.-third series. *The London, Edinburgh, and Dublin Philosophical Magazine and Journal of Science*, 14(90):1–22, 1857.

12 Massimo Sabbatini. Esa user guide to low gravity platforms, 2014.

13 Parabolic flight, 2024. URL https://www.nasa.gov/mission/parabolic-flight/.

14 Zero-g research programs, January 2024. URL www.gozerog.com/zero-g-research-programs.

15 Zero gravity research facility. URL https://www1.grc.nasa.gov/facilities/zero-g/.

16 The zarm drop tower in bremen. URL https://www.esa.int/Education/Drop_Your_Thesis/The_ZARM_drop_tower_in_Bremen.

17 Marit E. Meyer. Aerosol sampling experiment on theinternational space station. *47th International Conference on Environmental Systems*, 2017.

18 Stéphane Popinet. Gerris: a tree-based adaptive solver for the incompressible euler equations in complex geometries. *Journal of Computational Physics*, 190 (2):572–600, 2003.

19 Stéphane Popinet. An accurate adaptive solver for surface-tension-driven interfacial flows. *Journal of Computational Physics*, 228(16):5838–5866, 2009.

20 Alexis Berny, Luc Deike, Stéphane Popinet, and Thomas Séon. Size and speed of jet drops are robust to initial perturbations. *Physical Review Fluids*, 7(1): 013602, 2022.

21 A. Berny, S. Popinet, T. Séon, and L. Deike. Statistics of jet drop production. *Geophysical Research Letters*, 48(10), 2021.

22 Alexis Berny, Luc Deike, Thomas Séon, and Stéphane Popinet. Role of all jet drops in mass transfer from bursting bubbles. *Physical Review Fluids*, 5(3): 033605, 2020.

23 Qianbin Wang, Xi Yao, Huan Liu, David Quéré, and Lei Jiang. Self-removal of condensed water on the legs of water striders. *Proceedings of the National Academy of Sciences*, 112(30):9247–9252, 2015.

24 H. G. Andrews, E. A. Eccles, W. C. E. Schofield, and J. P. S. Badyal. Three-dimensional hierarchical structures for fog harvesting. *Langmuir*, 27(7):3798–3802, 2011.

25 M. Gürsoy, M.T. Harris, J.O. Downing, S.N. Barrientos-Palomo, A. Carletto, A.E. Yaprak, M. Karaman, and J.P.S. Badyal. Bioinspired fog capture and channel mechanism based on the arid climate plant salsola crassa. *Colloids and Surfaces A: Physicochemical and Engineering Aspects*, 529:195–202, 2017.

26 Zhao Pan, William G. Pitt, Yuanming Zhang, Nan Wu, Ye Tao, and Tadd T. Truscott. The upside-down water collection system of syntrichia caninervis. *Nature Plants*, 2(7), 2016.

27 Alexander A. Fedorets, Edward Bormashenko, Leonid A. Dombrovsky, and Michael Nosonovsky. Droplet clusters: nature-inspired biological reactors and aerosols. *Philosophical Transactions of the Royal Society A: Mathematical, Physical and Engineering Sciences*, 377(2150):20190121, 2019.

28 Weiwei Shi, Mark J. Anderson, Joshua B. Tulkoff, Brook S. Kennedy, and Jonathan B. Boreyko. Fog harvesting with harps. *ACS Applied Materials & Interfaces*, 10(14):11979–11986, 2018.

29 B Roman and J Bico. Elasto-capillarity: deforming an elastic structure with a liquid droplet. *Journal of Physics: Condensed Matter*, 22(49):493101, 2010.

30 Élise Lorenceau, Christophe Clanet, and David Quéré. Capturing drops with a thin fiber. *Journal of Colloid and Interface Science*, 279(1):192–197, 2004.

31 Keyvan Piroird, Christophe Clanet, Élise Lorenceau, and David Quéré. Drops impacting inclined fibers. *Journal of Colloid and Interface Science*, 334(1):70–74, 2009.

32 Emilie Dressaire, Alban Sauret, François Boulogne, and Howard A. Stone. Drop impact on a flexible fiber. *Soft Matter*, 12(1):200–208, 2016.

33 Jean Comtet, Bavand Keshavarz, and John W. M. Bush. Drop impact and capture on a thin flexible fiber. *Soft Matter*, 12(1):149–156, 2016.

34 A. Nasto, P.T. Brun, and A. E. Hosoi. Drop impact on hairy surfaces. *Physical Review Fluids*, 4(6):064004, 2019.

35 Francis W Minor, Anthony M Schwartz, EA Wulkow, and Lawrence C Buckles. The migration of liquids in textile assemblies: Part ii: the wicking of liquids in yams. *Textile Research Journal*, 29(12):931–939, 1959.

36 Bernard Miller, Arthur B Coe, and PN Ramachandran. Liquid rise between filaments in a v-configuration. *Textile Research Journal*, 37(11):919–924, 1967.

37 Raymond V Dyba and Bernard Miller. Evaluation of wettability from capillary rise between filaments. *Textile Research Journal*, 39(10):962–970, 1969.

38 H.M Princen. Capillary phenomena in assemblies of parallel cylinders. *Journal of Colloid and Interface Science*, 34(2):171–184, 1970.

39 C Py, R Bastien, J Bico, B Roman, and A Boudaoud. 3d aggregation of wet fibers. *Europhysics Letters (EPL)*, 77(4):44005, 2007.

40 S. Protiere, C. Duprat, and H. A. Stone. Wetting on two parallel fibers: drop to column transitions. *Soft Matter*, 9(1):271–276, 2013.

41 C. Duprat, S. Protière, A. Y. Beebe, and H. A. Stone. Wetting of flexible fibre arrays. *Nature*, 482(7386):510–513, 2012.

42 J. Bico, B. Roman, and A. Boudaoud. Elastocapillary coalescence in wet hair. *Nature*, 432:690, 2004.

43 Élise Lorenceau and David Quéré. Drops on a conical wire. *Journal of Fluid Mechanics*, 510:29–45, 2004.

44 Hélène de Maleprade, Matthias Pautard, Christophe Clanet, and David Quéré. Tightrope bubbles. *Applied Physics Letters*, 114(23):233704, 2019.

45 Serge Mora, Ty Phou, Jean-Marc Fromental, Basile Audoly, and Yves Pomeau. Shape of an elastic loop strongly bent by surface tension: Experiments and comparison with theory. *Physical Review E*, 86(2), 2012.

46 Johannes Schindelin, Ignacio Arganda-Carreras, Erwin Frise, Verena Kaynig, Mark Longair, Tobias Pietzsch, Stephan Preibisch, Curtis Rueden, Stephan Saalfeld, Benjamin Schmid, Jean-Yves Tinevez, Daniel James White, Volker Hartenstein, Kevin Eliceiri, Pavel Tomancak, and Albert Cardona. Fiji: an

open-source platform for biological-image analysis. *Nature Methods*, 9(7):676–682, 2012.

47 P. G. de Gennes. Wetting: statics and dynamics. *Reviews of Modern Physics*, 57(3):827–863, 1985.

48 Denis Bartolo, Christophe Josserand, and Daniel Bonn. Retraction dynamics of aqueous drops upon impact on non-wetting surfaces. *Journal of Fluid Mechanics*, 545(-1):329, 2005.

49 Daniel Bonn, Jens Eggers, Joseph Indekeu, Jacques Meunier, and Etienne Rolley. Wetting and spreading. *Rev. Mod. Phys.*, 81:739–805, 2009.

50 Sébastien Neukirch, Benoıˆt Roman, Benoıˆt de Gaudemaris, and José Bico. Piercing a liquid surface with an elastic rod: Buckling under capillary forces. *Journal of the Mechanics and Physics of Solids*, 55(6):1212–1235, 2007.

51 C. Raufaste, G. Kirstetter, F. Celestini, and S. J. Cox. Deformation of a free interface pierced by a tilted cylinder. *EPL (Europhysics Letters)*, 99(2):24001, 2012.

52 Bin Zhang, Vatsal Sanjay, Songlin Shi, Yinggang Zhao, Cunjing Lv, Xi-Qiao Feng, and Detlef Lohse. Impact forces of water drops falling on superhydrophobic surfaces. *Physical Review Letters*, 129(10):104501, 2022.

53 Yile Wang, Yage Zhao, Lijie Sun, Abbasali Abouei Mehrizi, Shiji Lin, Jianwei Guo, and Longquan Chen. Successive rebounds of impinging water droplets on superhydrophobic surfaces. *Langmuir*, 38(12):3860–3867, 2022.

54 Rachel E. Pepper, Laurent Courbin, and Howard A. Stone. Splashing on elastic membranes: The importance of early-time dynamics. *Physics of Fluids*, 20(8), 2008.

55 P.P. Sharma, S.C. Gupta, and W.J. Rawls. Soil detachment by single raindrops of varying kinetic energy. *Soil Science Society of America Journal*, 55(2):301, 1991.

56 T. Gilet and L. Bourouiba. Fluid fragmentation shapes rain-induced foliar disease transmission. *Journal of The Royal Society Interface*, 12(104):20141092, 2015.

57 Ghassan Hassan, Bekir S. Yilbas, Saeed Bahatab, Abdullah Al-Sharafi, and Hussain Al-Qahtani. A water droplet-cleaning of a dusty hydrophobic surface: influence of dust layer thickness on droplet dynamics. *Scientific Reports*, 10(1), 2020.

58 Denis Richard, Christophe Clanet, and David Quéré. Contact time of a bouncing drop. *Nature*, 417(6891):811–811, 2002.

59 Anne-Laure Biance, Frédéric Chevy, Christophe Clanet, Guillaume Lagubeau, and David Quéré. On the elasticity of an inertial liquid shock. *Journal of Fluid Mechanics*, 554(-1):47, 2006.

60 Christophe Clanet, Cédric Béguin, Denis Richard, and David Quéré. Maximal deformation of an impacting drop. *Journal of Fluid Mechanics*, 517:199–208, 2004.

61 Karl Cardin, Christophe Josserand, and Raúl Bayoán Cal. Droplet capture in a fiber array. *Physical Review Fluids*, 8(4):043601, 2023.

62 Hiroaki Katsuragi. Morphology scaling of drop impact onto a granular layer. *Physical Review Letters*, 104(21):218001, 2010.

63 G. Delon, D. Terwagne, S. Dorbolo, N. Vandewalle, and H. Caps. Impact of liquid droplets on granular media. *Physical Review E*, 84(4):046320, 2011.

64 Hiroaki Katsuragi. Length and time scales of a liquid drop impact and penetration into a granular layer. *Journal of Fluid Mechanics*, 675:552–573, 2011.

65 Heather N. Emady, Defne Kayrak-Talay, and James D. Litster. A regime map for granule formation by drop impact on powder beds. *AIChE Journal*, 59(1): 96–107, 2012.

66 E. Nefzaoui and O. Skurtys. Impact of a liquid drop on a granular medium: Inertia, viscosity and surface tension effects on the drop deformation. *Experimental Thermal and Fluid Science*, 41:43–50, 2012.

67 Song-Chuan Zhao, Rianne de Jong, and Devaraj van der Meer. Raindrop impact on sand: a dynamic explanation of crater morphologies. *Soft Matter*, 11(33): 6562–6568, 2015.

68 J.O. Marston, S.T. Thoroddsen, W.K. Ng, and R.B.H. Tan. Experimental study of liquid drop impact onto a powder surface. *Powder Technology*, 203(2):223–236, 2010.

69 T. Supakar, M. Moradiafrapoli, G.F. Christopher, and J.O. Marston. Spreading, encapsulation and transition to arrested shapes during drop impact onto hydrophobic powders. *Journal of Colloid and Interface Science*, 468:10–20, 2016.

70 Edward J. Long, Graham K. Hargrave, James R. Cooper, Ben G. B. Kitchener, Anthony J. Parsons, Caspar J. M. Hewett, and John Wainwright. Experimental investigation into the impact of a liquid droplet onto a granular bed using three-dimensional, time-resolved, particle tracking. *Physical Review E*, 89(3):032201, 2014.

71 Andrew P. Wollman. Capillarity-driven droplet ejection. Master's thesis, Portland State University, 2012.

72 F. Cabrera, M. Z. Sheikh, B. Mehlig, N. Plihon, M. Bourgoin, A. Pumir, and A. Naso. Experimental validation of fluid inertia models for a cylinder settling in a quiescent flow. *Phys. Rev. Fluids*, 7:024301, 2022.

73 T. Séon and G. Liger-Belair. Effervescence in champagne and sparkling wines: From bubble bursting to droplet evaporation. *The European Physical Journal Special Topics*, 226(1):117–156, 2017.

74 Gérard Liger-Belair. How many bubbles in your glass of bubbly? *The Journal of Physical Chemistry B*, 118(11):3156–3163, 2014.

75 Laurent Duchemin, Stéphane Popinet, Christophe Josserand, and Stéphane Zaleski. Jet formation in bubbles bursting at a free surface. *Physics of Fluids*, 14 (9):3000–3008, 2002.

76 Elisabeth Ghabache and Thomas Séon. Size of the top jet drop produced by bubble bursting. *Physical Review Fluids*, 1(5):051901, 2016.

77 Alfonso M. Gañán-Calvo. Revision of bubble bursting: Universal scaling laws of top jet drop size and speed. *Physical Review Letters*, 119(20):204502, 2017.

78 Alfonso M. Gañán-Calvo. Scaling laws of top jet drop size and speed from bubble bursting including gravity and inviscid limit. *Physical Review Fluids*, 3 (9):091601, 2018.

79 Luc Deike, Elisabeth Ghabache, Gérard Liger-Belair, Arup K. Das, Stéphane Zaleski, Stéphane Popinet, and Thomas Séon. Dynamics of jets produced by bursting bubbles. *Physical Review Fluids*, 3(1):013603, 2018.

80 Benjamin W. Zeff, Benjamin Kleber, Jay Fineberg, and Daniel P. Lathrop. Singularity dynamics in curvature collapse and jet eruption on a fluid surface. *Nature*, 403(6768):401–404, 2000.

81 Élisabeth Ghabache, Thomas Séon, and Arnaud Antkowiak. Liquid jet eruption from hollow relaxation. *Journal of Fluid Mechanics*, 761:206–219, 2014.

82 Adrien Benusiglio, David Quéré, and Christophe Clanet. Explosions at the water surface. *Journal of Fluid Mechanics*, 752:123–139, 2014.

83 Jeffrey M. Aristoff, Tadd T. Truscott, Alexandra H. Techet, and John W. M. Bush. The water-entry cavity formed by low bond number impacts. *Physics of Fluids*, 20(9), 2008.

84 Jeffrey M. Aristoff and John W. M. Bush. Water entry of small hydrophobic spheres. *Journal of Fluid Mechanics*, 619:45–78, 2009.

85 Raymond Bergmann, Devaraj van der Meer, Mark Stijnman, Marijn Sandtke, Andrea Prosperetti, and Detlef Lohse. Giant bubble pinch-off. *Physical Review Letters*, 96(15), 2006.

86 V. Duclaux, F. Caillé, C. Duez, C. Ybert, L. Bocquet, and C. Clanet. Dynamics of transient cavities. *Journal of Fluid Mechanics*, 591:1–19, 2007.

87 Stephan Gekle, José Manuel Gordillo, Devaraj van der Meer, and Detlef Lohse. High-speed jet formation after solid object impact. *Physical Review Letters*, 102 (3), 2009.

88 Raymond Bergmann, Devaraj Van Der Meer, Stephan Gekle, Arjan Van Der Bos, and Detlef Lohse. Controlled impact of a disk on a water surface: cavity dynamics. *Journal of Fluid Mechanics*, 633:381–409, 2009.

89 I. Kataoka. Local instant formulation of two-phase flow. *International Journal of Multiphase Flow*, 12(5):745–758, 1986.

90 Nathan C. Keim, Peder Møller, Wendy W. Zhang, and Sidney R. Nagel. Breakup of air bubbles in water: Memory and breakdown of cylindrical symmetry. *Physical Review Letters*, 97(14), 2006.

91 J. Eggers, M. A. Fontelos, D. Leppinen, and J. H. Snoeijer. Theory of the collapsing axisymmetric cavity. *Physical Review Letters*, 98(9), 2007.

92 S. T. Thoroddsen, T. G. Etoh, and K. Takehara. Experiments on bubble pinch-off. *Physics of Fluids*, 19(4), 2007.

93 Pierre Van de Velde, Suzie Protière, and Camille Duprat. Dynamics of drop absorption by a swelling fiber. *Soft Matter*, 17(25):6168–6175, 2021.